This is a peer-reviewed, accepted author manuscript of the following research article: Fardous, RS, Alshmmari, S, Tawfik, E, Khadra, I, Ramadan, Q & Zourob, M 2024, 'An integrated and modular compartmentalized microfluidic system with tunable electrospun porous membranes for epithelialized organs-on-a-chip', *ACS Applied Materials and Interfaces*, vol. 16, no. 31, pp. 40767-40786. https://doi.org/10.1021/acsami.4c08864

An integrated and modular compartmentalized microfluidic system with tuneable electrospun porous membranes for epithelialized organs-on-a-chip

Roa S. Fardous[ad], Sultan Alshmmari[bd], Essam Tawfik[c], Ibrahim Khadra[a], Qasem Ramadan[d], Moahammed Zourob[d*]*

(a) Strathclyde Institute of Pharmacy and Biomedical Sciences, Strathclyde University, Glasgow G4 0RE, United Kingdom

(b) Leibniz Institute of Photonic Technology, Albert-Einstein-Straße 9, 07745 Jena, Germany

(c) Advanced Diagnostics & Therapeutics Institute, King Abdulaziz City for Science and Technology, Riyadh 12354, Kingdome Saudi Arabia

(d) Alfaisal University, Riyadh 11533, Kingdome Saudi Arabia

Abstract:

A modular and 3D compartmentalized microfluidic system with electrospun porous membranes for epithelialized organ-on-a-chip systems is presented. Our novel approach involves direct deposition of polymer nanofibers onto a patterned polymethyl methacrylate (PMMA) substrate

using electrospinning, resulting in an integrated porous membrane (PM) within the microfluidic chip. The in-situ deposition of the PM eliminates the need for additional assembly processes. To demonstrate a high throughput membrane integration capability of our approach, we successfully deposited nanofibers onto various chip designs with complex microfluidic planner structures and expanded dimensions. We characterized and tested the fully PMMA chip by growing an epithelial monolayer using the Caco-2 cell line to study drug permeability. A comprehensive analysis of the bulk and surface properties of the membrane's fibers made of PMMA, and polystyrene (PS) was conducted to determine the polymer with the best performance for cell culture and drug transport applications. PMMA-based membrane, with a PMMA:PVP ratio of 5:1, allowed for the fabrication of a uniform membrane structure along the aligned nanofibers. By modulating the fiber diameter and total thickness of the membrane, we could adjust the membrane's porosity for specific cell culture applications. The PMMA-PVP nanofibers exhibited a low Polydispersity Index (PDI) value, indicating monodispersed nanofibers and a more homogeneous and uniform fiber network. Both types of membranes demonstrated excellent mechanical integrity under medium perfusion flow rates. However, the PMMA-PVP composition offered a tailored porous structure with modulable porosity based on fiber diameter and thickness. Our developed platform enables dynamic in vitro modelling of the epithelial barrier and has applications in drug transport and in vitro micro-physiological systems.

Keywords: Porous membrane, Electrospinning, Microfluidics, Integration, cell culture, PMMA, Compartmentalized.

1. Introduction

Over the past few years, there have been numerous technological advancements within the pharmaceutical industry that display immense potential to push the frontiers of pharmaceutical research to new vistas. The integration of various (bio-)engineering disciplines into the medical and pharmaceutical fields has enabled the application of engineering principles to tackle challenges in biology and medicine. Specifically, the infusion of advanced microfabrication, nanotechnology, and material science into the field of tissue engineering provided us with powerful tools for precise control over scaffold architecture, cell culture conditions, surface properties and delivery of bioactive materials [1, 2, 3, 4]. These advancements have significantly improved our ability to engineer functional tissues and organs in vitro for the purpose of regenerative medicine and to facilitate the exploration of the intra- and extracellular environment within the tissues. Organ-on-a-chip (OOC) and organoids models, which represent good examples of these advances, have a great potential to change the way of predicting patient responses to new molecules, paving the way for more effective drug discovery and development. OOC device is a microfluidic-based perfusion device that hosts a (co-)culture of cells in vitro and aims to recapitulate specific structure(s), function(s), and key aspects of human metabolism of a certain tissue or an organ in normal and pathological physiology [4]. OOCs enables dynamic long-term coculture of heterogenous cells arranged in precise under physiological perfusion conditions, hence promoting complex interactions between cells and the microenvironment. Microfabrication enables well-defined and precise features necessary for developing these living organs, such as the physiological microarchitecture, spatiotemporal cell-cell interactions, and extracellular microenvironments. Increasing the anatomical complexity of the organ-on-a-chip (OOC) system involves the incorporation of multiple cell types or tissues into a single OOC system. This requires

the design of complex multi-compartmental fluidic devices that enable efficient fluidic crosstalk between these compartments. This, in turn, facilitates the faithful replication of the complex interactions and responses observed in the human body. Porous membranes (PMs) play a crucial role in tissue engineering and OOC technology by providing a physical barrier that separates different cell populations and establishing apical and basolateral compartments while allowing for the exchange of nutrients, gases, and signalling molecules. These membranes are designed to mimic the natural extracellular matrix (ECM) of tissues and organs, facilitating cell growth and function [5].

PMs have become essential tools in the field of cell culture which are used as supports for epithelial/endothelial/epidermal cell culture to recapitulate various types of tissue barriers such as the intestinal epithelium [6, 7, 8], vasculature [10], lung [9], and skin [11]. In addition, cell culturing on both sides of the membrane is adaptable to microfluidic devices and allows cells exposure to controlled fluid flow, perfused drug or nutrients, chemical gradients, and physiological shear stresses [12, 13, 14, 15]. One of the primary applications of the PMs is studying the pharmacokinetics (PK) of drugs by measuring the transport of molecules through a constructed epithelial layer that resemble the main barrier of drug uptake (i.e., intestine, lung, and skin) and consequently studying the bioavailability and toxicity of the target compound. Therefore, the careful design and integration of PMs enables the creation of a more realistic and physiologically relevant microenvironment for studying complex biological processes and disease mechanisms.

PMs used in microfluidic devices are either fabricated, or assembled in the chip, using variety of materials including Silicon [17], Silicon Dioxide [18], Silicon Nitride [19, 20], Aluminum Oxide [26], Parylene [21], Polydimethylsiloxane (PDMS) [9, 22] and SU-8 [27] or commercially available track etched membranes such as Polycarbonate [23], Polyester [24] and phospholipid-

based biomimetic membrane [25]. To design a PM as a barrier structure in co-culture systems, a number of considerations, including pore size, porosity, thickness, fabrication materials and elasticity can impact the experimental control and physiological relevance. Optimizing these parameters is determined by the specific use of the membrane such as molecule transport between chambers (e.g., apical-to-basolateral transport), cell-cell communication through physical contact or biochemical communication, and transmigration (e.g., immune cell migration). In addition, surface modification of the membrane is used to control the cell attachment and optical transparency allows high resolution imaging during the experimentation [12, 16]. Polymeric membranes are commercially available in cell culture inserts with pore sizes ranging from 0.4 to 8 μm and thickness of 10 μm, or in free form with even smaller pore sizes. These membranes are fabricated using irradiation etching which leads to variation in the pore's density across the membrane surface. On the other hand, employing microfabrication techniques (e.g., lithography, chemical(wet) or physical (dry) etching) allows excellent control over the porosity, pore size, pore shape and thickness of the membranes. PDMS membranes are also commonly used in microfluidic devices for compartmentalization and cell culture support. To create a PDMS membrane, a negative template is fabricated using lithography technique and the template is used to mold the membrane with the PDMS polymer using soft lithography. PDMS is inherently hydrophobic, which can affect the behavior of cells and the adsorption of biomolecules on the membrane surface. Cell attachment and spreading may also be compromised which necessitates additional surface modifications to promote cell adhesion. Furthermore, PDMS has the ability to absorb small molecules (e.g., drugs) which might impact drug bioavailability testing.

Recently, electrospun nano/microfiber-based structures have been adopted, in a wide research community, as a potential alternative (bio-)fabrication material for biomedical applications

particularly, tissue engineering due to the ease of fabrication and low cost of production [28]. A plethora of research articles since then have proven the usability of electrospun fibrous scaffolds as permeable membranes for cell culture [28, 29, 30].

Electrospinning is well-established and has been described by numerous researchers [31, 32]. One important characteristic of electrospinning is that nanofibers can be produced using a wide variety of materials including natural and synthetic polymers [33]. The utility of electrospinning in fabrication of a variety of porous structures has been successfully demonstrated for various biomedical applications. However, there are many challenges that need to be addressed to enable the adoption of this process in the production of functional and robust biomaterials. Major challenges include large-scale fabrication and reproducibility like those currently commercialized counter structures and materials.

Electrospun fiber-based membranes have been fabricated using various polymeric materials including PDMS [34, 35], poly (ε-caprolactone) (PCL) [36, 38], Polyvinyl alcohol (PVA) [37], polystyrene (PS) [39], and a poly (lactic-co-glycolic acid) (PLGA) [40], and exploited for cell/tissue culture. However, integration of these membranes in microfluidic and OOC devices has only appeared recently. Moghadas et al 2017 and 2018 described a process of fabrication of PDMS-based flexible fibrous membranes and subsequent bonding to a PDMS microfluidic device [34, 35]. Following the electrospinning process, the membrane was bonded to the PDMS chip using plasma bonding and as a proof of concept, the membrane was used as a scaffold for culturing human lung cancer epithelial cells (A549 cell line).

The vast majority of the current lab-on-a-chip (LOC) and OOC devices have a simple structure, either planner or double-layered channels with a porous membrane and are fabricated using various unstandardized processes. However, OOCs are highly integrated systems by nature as they reflect

human physiology. In order to recapitulate a certain aspect of human physiology, a relatively complex engineering system with multi-compartments that hosts heterotypic cell co-culture and enables physiologically relevant tissue-tissue interaction is required. PMs are the key components in the fabrication of these compartmentalized systems. Integration of the PMs, which are usually made of different materials to the chip body, into the chips involves lengthy manual assembly which associated with notable chip-to-chip variations. In fact, there is a real need to tackle these technological challenges to facilitate scaling up OOC device production and transferring this technology from the laboratory bench to industry.

Fabricating a microfluidic device with all of its components in a single integrated sequential process is a critical step in fulfilling high throughput manufacturing requirements and transitioning this technology from the laboratory bench to production. This approach facilitates efficient and streamlined production, thereby enabling the mass production of microfluidic devices with consistent quality.

Here, we describe an innovative yet simple device and method that involves fabrication and integration of a compartmentalized microfluidic chip with a fiber-based PM for epithelialized OOC systems. The nanofibers that constitute the PM were directly deposited onto the chip using electrospinning eliminating any additional assembly process. The chip is fabricated of PMMA using laser machining and the PMMA or PS-based membrane were integrated in one simple process. To demonstrate a high throughput membrane integration, homogeneous deposition of the nanofibers was implemented on a variety of chip designs with complex microfluidic planner structures and expanded dimensions. Fig. 1a shows a schematic representation of the integrated device. The fully PMMA chip was characterized and tested by growing an epithelial monolayer using Caco-2 cell line for drug permeability.

2. Materials and Methods

2.1 Materials

PMMA sheets with thicknesses of 0.5 mm, 1 mm and 2mm were purchased from a local vendor. Double-sided adhesive (3M 467MP Adhesive Transfer Tape Acrylic 2.3 mil) is from 3M (Saint Paul, MN, USA). PMMA and PS pellets are from SABIC® (Riyadh, Saudi Arabia). N,N-dimethylformamide (DMF, 99%) was purchased from SABIC®, Polyvinylpyrrolidone (PVP) average Mw ~1,300,000 were purchased from Merck (Darmstadt, Germany).

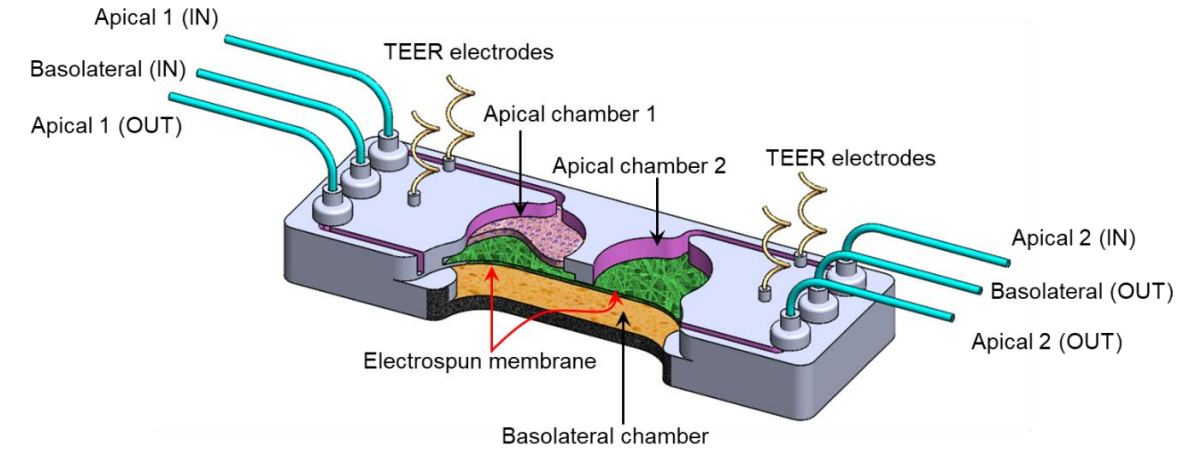

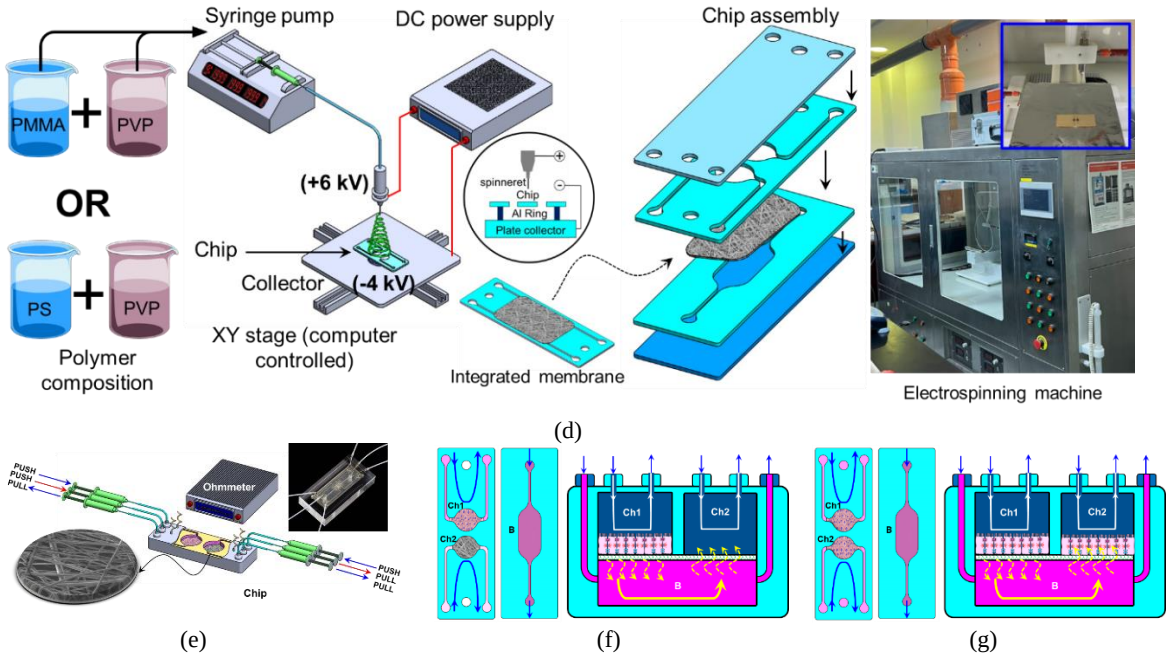

Figure 1: (a) A schematic representation of the integrated device showing the integration of the fiber-based porous mebrane into a compartmentlized microfluidic chip. The chip also comprises two integrated pairs of electrodes for TEER measurments. (b) The chip was fabricated of PMMA using laser machninig. Prior cutting, half of the sheet was laminated with a double-sided adhesive tape on to fabricated the two inner layers and to enable bonding the four layers togather. (c) Top view of the four layers with the PM is integrated into the apical layer. (d) Schamtic of the PM fabrication process and integration into the microfluidic chip (the electrospinning setup is shown on the right). (e) The fluidic setup during the chip testing include a two sets of syringes mounted on two programmble syringes pumps with a capability to modulate the flow rate and mode (push/pull). The electyrode are conneted to an Ohmeter for TEER measurments. (f) Schematic of the cell culture organization. The intestinal epithelial cells (Caco-2 cells) were grown in apical chamber 1 (Ch1) while cahmber2 (Ch2) kept cell free. The drawng also shos the flow direction through the multi-compartments. (g) Caco-2 cells were grown in both apical chambers (Ch1 and Ch2).

Human colorectal adenocarcinoma cells (Caco-2) are from American Type Culture Collection (ATCC) (Manassas, VA, USA). Poly-L-lysine (PLL) solution, 0.1 % (w/v), collagen (type 1, rat tail) and Trypsin/EDTA were purchased from Sigma Aldrich (Burlington, Massachusetts, USA). Dulbecco's Modified Eagle Medium/Ham's F-12 (DMEM/F12) containing 10% (v/v) fetal bovine serum and 1 % penicillin-streptomycin antibiotic was purchased from Gibco, AlamarBlue ™ Cell Viability Reagent were from Thermo Fisher Scientific (Waltham, Massachusetts, USA).

2.2 Preparation of the PMMA and PS polymer solutions

PMMA pellets were dissolved in DMF to obtain 10, 11, 22, and 33 %w/v concentrations and the solution was stirred continuously overnight at 500 rpm and 50 °C. Then, PVP was added with concentrations corresponding to 10, 2, 2, and 2 %w/v to produce the PMMA-PVP polymeric solution. The complex was then mixed for 5 hours before loading into the electrospinning apparatus. Similar procedures were applied to produce the PS-PVP polymeric solution. The dynamic viscosity of the polymer solutions was measured by DV3T viscometer (Brookfield, USA) at speed of 15rpm and temperature of 25°C.

2.3 Device fabrication

2.3.1 Micromachining of the PMMA-based chip

The microfluidic chip was fabricated using laser machining technique (Fig. 1b). The chip was firstly designed using AutoCad software (Autodesk, San Francisco, California, USA) and the file was then transferred to the laser cutter (Beambox, Flux, Taipei, Taiwan) using the Beam Studio software. To create a fully sealed microfluidic system, the chip was fabricated out of four PMMA layers (two inner layers and two outer layers) (Fig. 1c) which are then bonded together using a double-sided adhesive tape. To fabricate the two inner layers, a 1mm thick PMMA sheet, with dimensions of 50 × 30 cm^2, was laminated on both sides with a double-sided adhesive tape and cut with the laser machine while un-laminated sheets were used to cut the outer layers (Fig. 1b). The chip comprises one lower (basolateral) chamber/channel and two upper (apical) chambers where the fibers were deposited (Fig. 1c). The resultant fluidic volume of the basolateral chamber is 84 µL, while the volume of each of the apical chamber is ~20 µL. To facilitate cells and reagent injection and sample collection, PEEK tubings with an inner/outer diameter of 0.5 mm/1mm were

connected to the chip through a custom-fabricated fluidic nuts which were 3D printed using ASIGA MAX UV 3D printer (NSW, Australia) (Fig. 1a and e).

2.3.2 The porous membrane fabrication (electrospinning)

The membranes were electrospun using a biomedical electrospinning equipment (TL-BM) from Tong Li Tech (Shenzhen, China) which is equipped with positive and negative high voltage supply, 4-channel syringe pump and robotic control of spinnerets and collectors. Prior to loading the polymer solution into the electrospinning apparatus, the spinning parameters were adjusted as listed in table 1. The collector displacement during the spinning process was optimized and programmed to produce a specific nanofiber membrane pattern that ensures full coverage and homogeneous fiber density across the targeted chamber.

Table 1: Electrospinning setup parameters.

Parameter	Value
Ambient temperature	30 °C
Humidity	20%
Nozzle-to-collector distance	5 cm
Nozzle inner diameter	19 gauge (0.9 mm)
Flow rate	0.5 mL/h
Voltage between voltage spinneret and collector	10 kV
Collector travelling coordinates X/Y	100 mm/5mm
Collector velocity	5 mm/s
Work acceleration	5mm/s^2
Corner-to-corner acceleration	40 mm/ s^2
Spinning duration	4 hours

The apical PMMA layer with its bottom facing up was placed on the collector which was covered with an aluminum foil (Fig. 1d). To encourage the fiber deposition onto the PMMA surface of the chip which has low conductivity, an aluminum ring was placed underneath the PMMA layer, which serves as a focusing electrode, in order to create a high charge density around the edges of the fluidic chamber where the membrane need to be deposited. The sharp edges of the aluminum

ring increase the number of localized electric charges and create a non-uniform electric field at the surface of the ring. The size of aluminium ring (diameter = 20 mm) was chosen to be larger than the area of the chamber to avoid nonuniformity of the fiber deposition. Under a strong electric field, the insulating substrate (PMMA) of the chip will be polarized and consequently render it a part of the collector. The negative charges applied on the collector also provide an additional pulling force of the electrospinning jet, hence encouraging the deposition of the fibers on the surface of the chip and covering the targeted chamber. The total acting force on a charged element in the electric field can be written as F=qE, where E is the field strength and q the magnitude of the charged element. In this setup, the charged jet would stretch across the periphery of the ring and the field lines are attracted towards the ring. The polymeric composite which consists of PMMA (22% w/v) and PVP (2% w/v) solution with a specific PMMA:PVP ratio was loaded into a 20 mL plastic syringe fitted with PTFE tubing and controlled by a syringe pump. The syringe was then connected to a single nozzle dispensing needle with steel blunt tip and size of 19 gauge through a Teflon tube. After optimization, the spinneret-collector voltage was set at 10 kV where the collector voltage was -4 kV and the distance between the spinneret and collector was set at 50 mm. The polymer flow rate was adjusted to 0.5 mL/h and the electrospinning process was maintained at a humidity of 20% and a temperature of 30 °C in a dust-free cabinet.

2.3.3 Chip assembly

After the membrane deposition on the apical layer, the four layers were bonded together to form the 3D chip with a porous membrane as shown in Fig. 1d and e. Another key component in the device is the TransEpithelial Electrical Resistance (TEER) electrodes which are used to measure the changes in resistance to the paracellular ion transport as an indicator of epithelial integrity. Two Ag/AgCl wires with diameter of 0.5 mm (Prime Bioscience Pte Ltd, Singapore) were inserted

through holes were created during the laser cutting to access the apical and basolateral sides of the cell culture. The first wire was inserted into the apical side of chamber 1 and accessed the basolateral side, the second wire was inserted into the apical side of chamber 2 (Fig.1a). A set of PEEK tubing with an inner/outer diameter of 1/32" (0.79 mm)/1/16" (1.57 mm) were connected to the fluidic ports of the chip. To ensure leakage free flow, the tubes were tightly fitted in 5 mm PMMA nuts fitted with silicone tubes as shown in Fig. 1a.

2.4 Characterization of the porous membrane

SEM Imaging: The nanofiber membrane morphology was characterized with a field emission Scanning Electron Microscope (SEM), JSM-IT500HR, In TouchScope™ (JEOL, Pleasanton, CA, USA) which is controlled by SMILE VIEW™ Lab software. Samples were initially sputter-coated with 2 nm of platinum and placed on the holder. The orientation of the sample was adjusted to obtain the best top view of the membrane. For cross-sectional imaging, the membrane was cut in half and placed on the holder in a direction vertical to the SEM viewing axis to enable the membrane thickness measurement. The SEM images were produced using electron field of 5 kV. The individual fiber size and the resultant pore sizes were extracted from the SEM images and analyzed using ImageJ software. The membrane thickness and porosity were assessed by analysing a number of electrospun membranes with different electrospinning time. Dynamic light scattering (DLS) is utilized to support the zeta potential and nanofibers diameter characterization. DLS measurements were performed using Malvern Zetasizer Nano ZS (Malvern Instruments Limited, Malvern, Worcestershire, UK). Toluene 10% was used as dispersant for nanofibers at 0.1 g/5 mL in toluene. XRD pattern analysis was taken by (Rigaku miniflex600) using CuKα radiation [30Kv, 40mA, 1.54430A°] between 0-80°, to identify the “fingerprint” of polymeric nanofibrous composites. The full width at half-maximum height (FWHM) of the diffraction peaks was

calculated by fitting the X-ray diffraction data with a Gaussian-Lorentzian function (Origin 8.5 software, Origin Lab, USA). The UV/visible optical absorption properties of PMMA-PVP and PS-PVP integrated membranes were assessed using a (Thermo Scientific GENESYS 10 UV) scanning instrument.

FTIR analysis: To investigate the chemical composition of the PMMA-PVP and PS-PVP fibares, FTIR analysis was performed using Nicolet iS10 FTIR spectrometer (ThermoFisher Scientific, USA). The FTIR spectra at transmittance mode were recorded in the range of 4000–500 cm^{-1} with an average scan of 300 at a resolution of 4 cm^{-1}.

Contact angle measurements: To characterize the wettability of the nanofibrous, the contact angle which is formed by a liquid at the three-phase boundary where liquid, gas, and solid intersect, was measured by capturing high resolution images of a water droplet using a digital camera (Nikon D7500) equipped with zoom lenses (18–200 mm). The electrospun membrane (PMMA, PMMA-PVP, PS and PS-PVP) was placed on a clean and flat solid surface. A small MQ water droplet was dispensed in vertical direction on top of the membrane using a micro-syringe with a capacity of 5.0 μL. The needle tip was set 5 millimeters away from the surface of the membrane. The droplet size was successfully small to ensure that the gravity effect would be insignificant. Then a high-resolution image was captured, and the contact angle was measured using the ImageJ software. For each membrane type, three samples were tested. Experiments were conducted at room temperature.

Differential scanning calorimetry (DSC): Thermal analysis of PMMA-PVP and PS-PVP nanofiber membranes was carried out using a DSC (Hitachi DSC7020, CA, USA). Samples with mass of (5–10 mg) were analyzed from (-20°C to 350 °C) at a heating rate of 5°C/min under a nitrogen flow of 50 ml/min.

UV/Visible measurement: The UV/visible optical absorption properties of embedded PMMA-PVP and PS-PVP fiber mats were assessed using Lambda 25 ultraviolet-visible spectrometer (PerkinElmer, USA). The recorded spectrum was within the range of 200-800nm.

Mechanical characterization of the membrane: The elastic modulus and hardness of the electrospun membranes were measured using the NanoTest Vantage, (Micromaterials, UK). Berkovich type diamond indenter was used with a maximum load of 0.5 mN.

2.5 Perfusion setup and pre-culture chip preparation

The fluidic inlets/outlets of the chip were connected to six syringes each has a volume of 10 mL fitted with18gauge blunt needle which are driven by two syringe pumps (SP230iwZ, World Precision Instruments, WPI, UK) as shown in Fig. 1e. The fluid was injected into each apical chamber through one syringe by setting the syringe pump at the PUSH mode, while the other syringe connected to the outlet was driven by the second syringe pump which runs at PULL mode. In the same manner, the fluid was injected into the basolateral chamber by one syringe running with PUSH mode and leave the chamber through a second syringe running with PULL mode (Fig. 1e). With this setting, fresh culture media are continuously introduced into the three chambers using three independent syringes and extracted out through another three syringes. The flow rate through all the syringes in all experiments was set as 10 nL/s. The extracted supernatants in the outlet syringes were collected and kept at -20° C for later analysis. Prior cell culture experiments, the microfluidic chip and all fluidic and fitting components were sterilized with 70% ethanol and exposed to UV light for 1 hour. Then, the chip was flushed with sterile water at a flow rate of 10µl/min for 1 hr and filled with the cell culture media and incubated in the CO2 incubator for 24 hrs. To promote natural cell adhesion onto the membrane and to encourage cell proliferation, the membrane was treated with Poly-L-Lysine (PLL) solution (0.1% (w/v). Then 50µL was injected

into each apical chamber and incubated for 5 minutes followed by gente washing with sterilized water. Then, the membrane was treated with collagen type 1 (50 μL, 0.02% (w/v)) for 2 hrs at room temperature followed by incubation at 37 °C for 30 min. PLL is relatively stable to shear stresses and enhances electrostatic cellular interaction, while collagen 1 fills the gaps between electrospun nanofibers and flattens the surface of the membrane for better monolayer cell growing. The membranes were washed with PBS before cell seeding.

2.6 Fluidic characterization

The microfluidic device comprises two apical chambers linked through one long basolateral chamber with a porous membrane (Fig.1a). To visualize the flow profile in the device, colored water was injected into the first apical chamber and the infusion of the color into the basolateral and the second apical chamber was monitored over time. The device was also subjected to long perfusion (up to one week) at different flow rates (from 50 μL/min to 500 μL/min) to monitor the stability of the membrane under different flow conditions. In addition, the crosstalk between the three fluidic chambers was examined by monitoring the permeability of 40 kDa dextran molecules. 10 μg/ml of FITC-dextran was injected through the first apical chamber and the transmembrane flux of the FITC-dextran was measured by serial sampling of a fixed volume from the basolateral and second apical chambers at different time intervals. The tracer concentration was measured using FilterMax F5 fluorescent plate reader (Molecular Devices, USA).

2.7 Cell culture

The epithelium of the human small intestine was modeled in vitro by constructing a confluent layer of Caco-2 cells (American Type Culture Collection (ATCC) Manassas, VA). Caco-2 cells (passages 6-11) were grown on 25 mL tissue culture flasks in DMEM/F-12 cell culture media with high glucose and with 10% (v/v) fetal bovine serum (FBS) and 1 % penicillin/streptomycin

antibiotic at 37 °C, 5% CO2 in 95% relative humidity (RH) till reaching 80% confluence. Culture medium was refreshed every 2 days and cells were harvested by passaging Trypsin/EDTA solution.

Testing the biocombatibility of the membranes: To examine any possible cytotoxic effect of the electrospun membrane for cell culture usability, cells were initially cultured in a 96-well culture plate at a density of 5×10^4 cells/well. Electrospun nanofibers were grinded and mixed with fresh culture media at concentrations of 25, 50, 250, 500 and 1,000 μg/mL. Ater 24 hrs of culture, the media were replaced with fresh media suspended with nanofiber powder with the above concentrations with a total volume of 200 μL/well and incubated for 48 hrs of incubation. The cell viability was examined using Alamar blue assay. Briefly, the culture media in each well was replaced with a fresh solution mixed with 100 μL (10% (v/v)) of Alamar blue solution and incubated for 3 h at 37 °C. Fluorescence was read at excitation/emission of 560 nm/600 nm) using the Cytation 3 Cell Imaging Multi-Mode Reader (Agilent Technologies, USA). The data were analyzed by calculating the percentage of Alamar blue fluorescence intensity and expressed as a percentage of the untreated control (UTC) and positive control Triton X-100 (10%). Results are presented as mean ± standard deviation of experiments performed in triplicate.

Cell culture on chip: Prior cell seeding, the chips were sterilized with 70% ethanol and exposed to UV light for 1 hour. The chip was filled with fresh culture media and incubated for 24hrs. Then, the medium in the apical chamber was replaced with Caco2 cell suspension at a concentration of 2.5×10^5 cells/mL (i.e., on top of the fibrous membrane). Fresh medium was also injected into the basolateral chamber. Subsequently, the chips were placed inside the CO2 incubator and the cells were allowed to attach for 24 hrs with the absence flow. The following day, the perfusion was switched ON as described above. Chips with a commercial polyester (PET) membrane with a pore

size of 0.4 µm which was cut out from a transwell insert (Corning, New York, USA) were also used as a control.

The design of the chip with two apical chambers (Ch1 and Ch2) and two membranes (M1 and M2) allow a versatile cell co-culture setup for studying cell-cell communication, pharmacokinetics, etc. To demonstrate this versatility, cell culture was implemented in two configurations as examples of its usability as shown in Fig. 1g and h:

- In the first configuration cells were grown only in one apical chamber (Ch1) on top of the membrane M1 (Fig. 1f). A confluent monolayer of caco-2 cells was grown on M1and cell products were monitored in the basolateral chamber and the second apical chamber. The permeability through the epithelial monolayer was examined by treating the cells in Ch1 with FITC-dextran and the infiltrate was collected from Ch2 and the basolateral chamber. The TEER electrodes were inserted in the two apical chambers where one electrode accesses the apical side of the monolayer while the second electrode accesses the basolateral side of the cells.
- In the second configuration, cells were grown on both M1 and M2 (Fig. 1g) and the permeability was measured through the two constructed monolayers by measuring the FITC-dextran permeate through the first monolayer in the basolateral chamber and through the second monolayer in the second apical chamber Ch2.

Immunofluorescence staining of intercellular tight junctions: The formation of the intercellular tight junctions (TJs) was detected by immunofluorescence staining once a confluent monolayer was established. In parallel, TEER measurement was also conducted. The cells were washed with 1× PBS and fixed with 4% paraformaldehyde (PFA) (Catalog #P6148, Sigma) and incubated for 15min, followed by another washing step with 1× PBS. Then the cells were

permeabilized with 0.25% Triton X-100 (Catalog #X100, Sigma) in 1× PBS by incubating the sample for 10min followed by another washing step. Non-specific binding sites were blocked with 5% bovine serum albumin (BSA) (Catalog #A2153, Sigma) in 1× PBS for 30min. Then, the sample was incubated with 2 µg/mL anti-mouse occludin antibody (Catalog# 331500, Life Technologies) overnight at 4 °C. The sample was then washed with PBS and treated with 3 µg/mL anti-mouse IgG conjugated to FITC (Catalog# 339111, Life Technologies) for 1 h in the dark at room temperature. The samples were then washed with 1ml of 1× PBS. The cells were inspected using fluorescent microscope (CKX53, Olympus, Tokyo, Japan) equipped with high resolution CCD camera.

Apical-to-basolateral permeability measurement: The apical-to-basolateral flux (permeability) of FITC-dextran (40 kDa) were studied in two cellular systems (1) One epithelial monolayer: The indicator, with a concentration of 10 µg/mL, was injected into the apical compartment (with cells) and samples were collected from the basolateral compartment beneath the cells and from the second apical compartment above the second membrane. In this configuration the indicator passes through the epithelial barrier and the PM, and the sample is labelled (M-C1). Then, it continues to pass through the second membrane (without cells) and the sample is labelled (M-C1-M2). M refers to membrane and C refers to cells 1 and 2 refer to first and second, respectively. (2) Two epithelial monolayers: The indicator is also injected into the apical compartment (with cells) and samples were collected from the basolateral compartment beneath the cells and from the second apical compartment above the second monolayer. In this configuration the indicator passes through the epithelial barrier and the PM, and the sample is labelled (M-C1). Then, it continues to pass through the cell monolayer, however through basolateral-apical route, and the sample is labelled (M-C1-M2C2). In parallel, the study has been conducted on another set of chips with the commercial PET

membrane to compare both systems with different membranes. The tracer concentration was measured using Enspire fluorescent plate reader (Perkin Elmer, USA)

2.8 Drug testing (Metformin)

Drug testing experiments were conducted after 14 days of cell culture by ensuring the cells are fully confluent and fully differentiated by TEER measurements and microscopic observation. The chip at this stage was connected to a tight fluidic circuit for continuous perfusion as described in section 2.5. The metformin was diluted in the culture media at a concentration of 100 µg/mL. The medium perfusion into the apical chamber was switched OFF to enable drug treatment. Using a pipette, a100 µL of the metformin-loaded medium was injected into the apical chamber and the perfusion into the apical chamber was switched ON after 20 min. Samples from the basolateral chamber were collected in a time-resolved manner which eliminate any cell culture disruption thanks to the continuous perfusion. The uptake of the drug in the basolateral side of the cells was analyzed using High Performance Liquid Chromatography (HPLC) technique. The apparent permeability coefficient (Papp) of the drug was calculated using the following equation [41]:

$$P_{app} = \frac{dQ}{dt} \times \frac{1}{A.C_0} \quad (1)$$

Where dQ/dt is the amount of solutes flux across the caco-2 barrier in time dt, A is the surface area of the epithelium in contact with apical solution and C0 is the initial donor (apical) concentration.

3. Results and Discussion

3.1 Effect of the chemical composition & the rheological properties of the polymer and electrospinning conditions on the fiber & membrane morphology

The aim of the study is to construct a nanofiber-based porous membrane with improved cell affinity and permeability, as well as reduced hydrophobic molecules absorption within a 3D

microfluidic device. Non-charged water-soluble PVP was chosen as an addition to increase the wettability and control the hydrophilicity of PMMA nanofibers. In order to fabricate well-defined nanofibers of PMMA-PVP polymeric composite, the concentration ratio for the combination varied with different viscosities, and their effects on the morphology of the obtained fibers were investigated. PVP with a hydrophilic nature interacts with PMMA and dissolves well in water and a variety of organic solvents [42, 43]. Furthermore, PVP and PMMA possess interacting chemical groups (carbonyl and amide groups, respectively) that may allow for strong interaction with high miscibility as well as crosslinking control [44]. Combining PMMA and a water-soluble polymer leads to improved wettability and surface hydrophilicity while retaining the fiber's hydrophobic elastic/mechanical structure.

Initial work of membrane fabrication was conducted utilizing PMMA- and PS-based solutions containing varying PMMA/PS:PVP ratios, as elucidated in section 2.2, to optimize the conditions for producing the desired membrane's structure and morphology. Moreover, the primary electrospinning parameters, including polymer viscosity, applied voltage, polymer flow rate, and needle-collector distance were optimized to achieve a combined effect encouraging the production of a membrane quality allowing its rational use as a permeable substrate for epithelial cell culture. The membranes were fabricated and characterized on multiple chips (i.e., onto the basolateral/apical layer (Fig. 1c)), and the qualities of the resultant membranes from both polymers were compared (Fig. 2). The effect of the viscosity on the morphology of the electrospun fibers was investigated by preparing PMMA:PVP at different concentrations of polymer. The viscosity of each solution was measured prior to electrospinning. Fig. 2a shows SEM images of the electrospun fibers taken at various viscosities from low to high. The viscosity of the polymer solution affects the behavior of the polymer jet and the subsequent solidification of the fibers,

therefore plays a crucial role as a dominant parameter in determining the morphology of the electrospun fibers [45]. Very low viscosity can interrupt the polymeric filaments that leads to producing disconnected fibers hence, producing nonhomogeneous fibrous structure with many voids. At low viscosity (e.g., 438 mPa.s) there was a tendency to form spherical-shaped beads along the fibers (Fig. 2ai). As the viscosity progressively increases, the bead's shape tends to transform to be spindle-like and the distance between beads on the fiber increases (Fig. 2aii, iii). At high viscosity (e.g., 2,688mPa.s) the beads disappeared to finally form uniform and aligned fibers (Fig. 2aiv). The formation of beads along the fibers may be attributed to the capillary breakup of the electrospun jet due to the surface tension in the presence of electric field [46]. Further increase in the viscosity (e.g., 6,938 mPa.s) would interrupt the polymer filament.

Viscosity (mPA.s), PMMA:PVP (10:1)

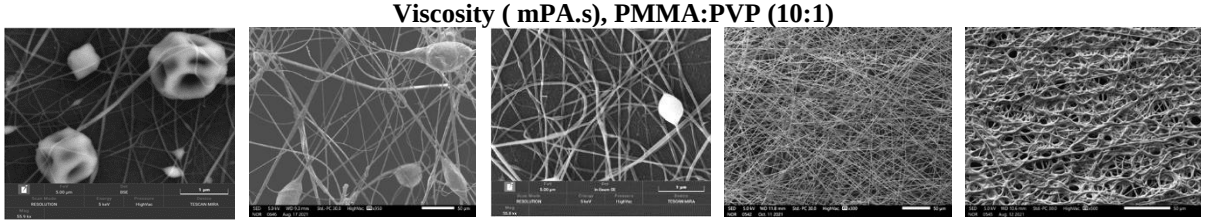

(i) μ= 438 (ii) μ=687.5 (iii) μ=1,238 (iv) μ=2,688 (v) μ=6,938

(a)

Voltage, PMMA:PVP (10:1)

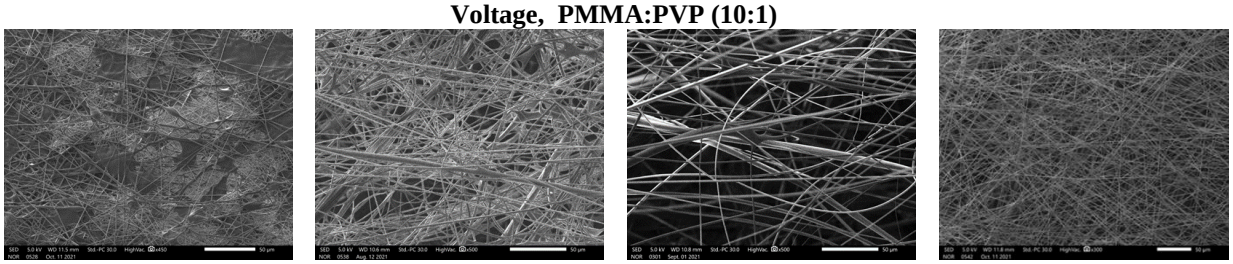

(i) V= 2kV (ii) V= 4kV (iii) V= 8kV (iv) V= 10kV

(b)

PMMA:PVP Viscosity	PMMA-based fibers	Observations	PMMA:PVP 5:1	PS:PVP 5:1
1:0 6,938	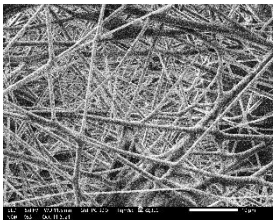	Very thick fibers. Unaligned and melted fiber bundles with polymer residuals	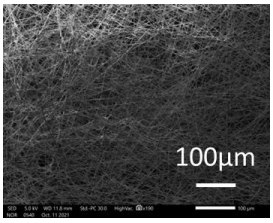	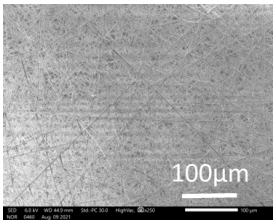
10:1 (6,745)	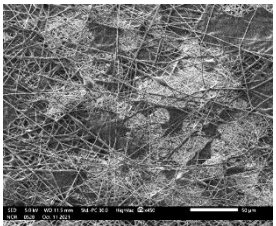	Thick and beaded fibers. Hydrophobic membrane.	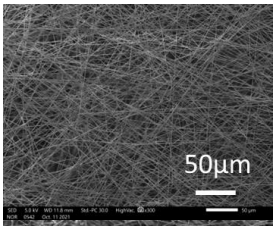	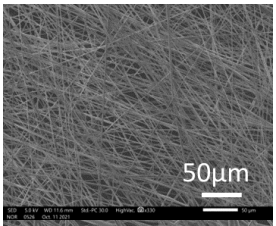
5:1 3,323 ✓	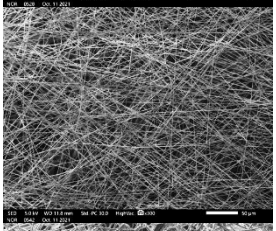	**Aligned, beadless and uniform nanofibers.**	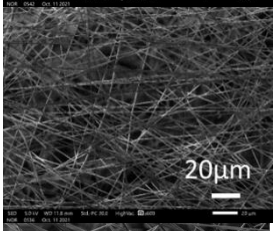	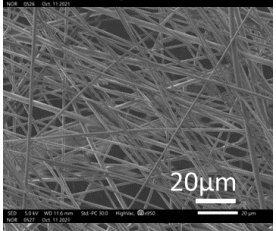
1:1 2,688	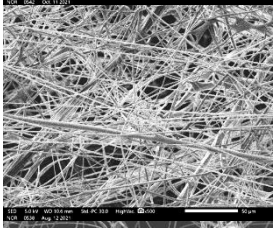	Non-uniform fiber mesh. The membrane was partially dissolved in water.	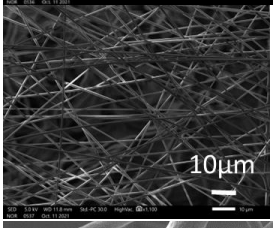	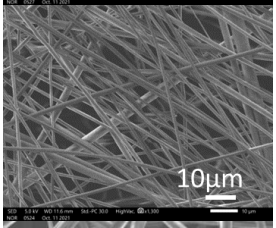
1:5 687.5	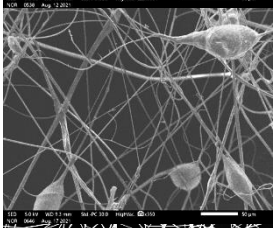	Beaded and discontinuous nanofibers. Low density fibers with large voids	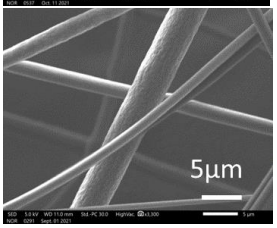	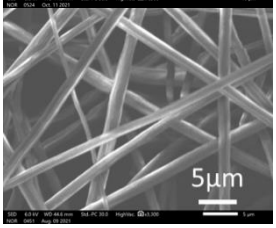
0:1	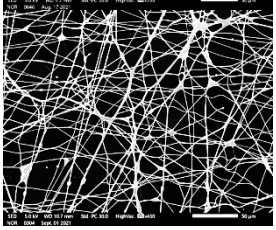	The fibers were too hydrophilic. Fibers were dissolved in water emmidiatly.		

(c) (d)

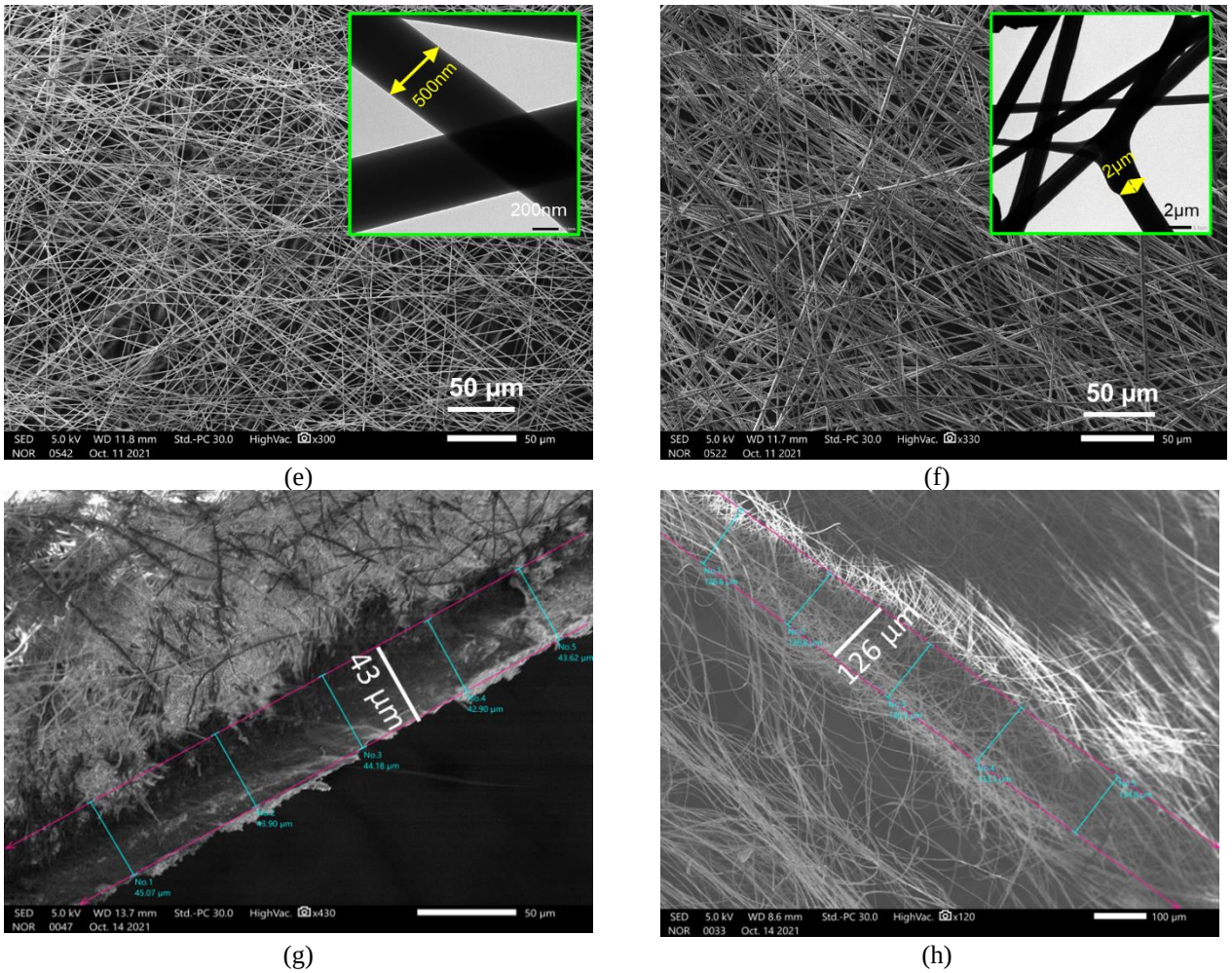

(e) (f)

(g) (h)

Figure 2: (a) SEM images of PMMA-PVP nanofibers at different viscosities with PMMA:PVP ratio of 10:1. High viscosity solutions tend to produce more aligned fibers, while lower viscosity solutions result in randomly oriented fibers. The viscosity affects the morphology of the individual electrospun fibers which consequently affect the overall structure morphology. (b) SEM images of PMMA-PVP nanofibers at different applied voltages. Continuous thin fibers with a uniform overall structure were formed at applied voltage of 10 kV. Less uniform structures with many voids were observed at low voltages (e.g., 2-8 kV). (c) SEM images of PMMA-PVP at different PMMA:PVP ratios. increasing of the PMMA:PVP ratio, showed significant enhancement of the fiber and overall structure quality. At a ratio of 5:1 improved jet stability was obtained, and the morphological appearance transferred from polymer solution droplets to continuous, aligned, and beadless fibers forming a uniform nanofibrous membrane. (d) SEM images of PMMA:PVP and PS:PVP with different magnifications. The PMMA-PVP mesh-like membrane has less density than PS-PVP and smaller nanofiber diameter sizes as well. The pore size of the PMMA-based membrane is larger than that of the PS-based one which correlates to the overall porosity of the membrane. (e-f) SEM images of the PMM- and PS-based membrane, respectively after the final optimization of the chemical composition and electrospinning conditions. TEM images of single fibers are shown in the insets. (g-h) The measured thickness of the PMMA- and PS-based membranes.

At higher viscosity solutions, the polymer tends to resist the extruding and stretching which lead to forming thicker and unaligned fibers which appeared as melted and stacked filaments (Fig.2av). In general, high viscosity solutions tend to produce more aligned fibers, while lower viscosity solutions result in randomly oriented fibers. In addition, viscosity can affect the morphology of the individual electrospun fibers which consequently affect the overall structure morphology and surface and bulk properties. The applied voltage together with the needle-collector distance, electrical conductivity and surface tension of the solution also influence the fiber formation and morphology. Fig. 2b shows SEM images of nanofibers spun at different applied voltages. It was observed that continuous thin fibers with a uniform overall structure were formed at applied voltage of 10 kV. However, less uniform structures with many voids were observed at low voltages (e.g., 2-8 kV). Higher voltage enhanced the probability of bead formation, particularly when combined with low viscosity solution. Next, polymer solutions with different ratios of PMMA:PVP and PS:PVP were prepared. The polymer ratios within the solution shows to influence the diameter of the individual electrospun fiber and the overall morphology of the bulk structure which was confirmed by the SEM and TEM microscopic observations (Fig. 2c-f). Using pure PMMA solution (i.e., without PVP) resulted in a thick and non-uniform fibrous structure with irregular fiber density across the membrane. Unspun polymer residuals also were observed (Fig. 2c top panel). The resulting membrane was hydrophobic as it imposes high resistance to water diffusion when applied on the apical surface. Cell adhesion can be compromised by hydrophobic surfaces, and this can lead to the detachment ofcells or inconsistent confluency. When a ratio of 10:1 was used, relatively very thick fibers (~2-5µm) were obtained (Fig. 2c, second panel). Also, the fibers appeared as stacked/melted and unaligned bundles with patchy polymer residuals. The density profile of the fibers was not uniform, such that the resulted structure is non-porous at

specific zone while highly porous, with large pores, at other zones. Progressive increasing of the PMMA:PVP ratio, showed significant enhancement of the fiber and overall structure quality. At a ratio of 5:1 (viscosity of 3,323 mPa.s, improved jet stability was obtained. Consequently, the morphological appearance transferred from polymer solution droplets to continuous, aligned, and beadless fibers forming a uniform nanofibrous membrane with an average fiber's diameter of 727 (±80) nm and a pore size of approximately 4.5 μm. Also, the fibers density in the overall structure (i.e., the membrane) becomes uniform with the absence of large voids. At a ratio of 1:1, the polymeric solution tends to form non-uniform micro/nanofibers and dissolves rapidly in media within 30 seconds due to a hydrophilic-hydrophobic balance (HHB), as the hydrophilic portion is similar in quantity to the hydrophobic portion. The solubility of fibrous structures increases due to the association of hydrophilic heads with water molecules. Furthermore, at this particular ratio, the fibrous structure becomes less uniform, and large voids start to emerge. Further increase of the PVP within then solution, resulted in beaded and discontinuous fibers with larger voids (i.e., low fibers coverage). Also, increasing the PVP concentration transforms the fibrous structure to become highly hydrophilic which negatively affects the stability of the structure as evidenced by rapid dissolving of the fibers in water. It is not trivial to predict the influence of all the above parameters on the resulting morphology of the individual fibers and the bulk structure because it depends on the combination of these parameters. Therefore, the empirical data retain an important role in determining the optimal conditions to gain high quality electrospun fibers. Table 2 lists the selected values within the suitable ranges.

Table 2: Zeta potential, hydrodynamic diameter of the nanofibers

Nanofibrous Membrane	zeta-potential (ζ, mV)	Polydispersity Index (PdI)	Hydrodynamic diameter (D_H, nm)	SEM average diameter (D_{av}, nm)
PMMA-PVP	+95.9 ± 6.5	0.47 ± 0.16	955.4 ± 41.5	727 ± 80
PS-PVP	+47.3 ± 8.2	0.81 ± 0.17	1,281 ± 50	1,100 ± 95

From the SEM images, the optimum ratio of PMMA:PVP was found to be 5:1 which allows fabricating a uniform membrane structure along the aligned nanofibers. This ratio was selected to pursue the membrane fabrication using both PPMA- and PS-based membrane at the same other electrospinning conditions. As shown in Fig. 2d, the PMMA-PVP mesh-like membrane has less density than PS-PVP and smaller nanofiber diameter sizes as well. In addition, the pore size of the PMMA-based membrane is larger than that of the PS-based one which correlates to the overall porosity of the membrane. The assembly of larger fibre diameter would result in less fiber density, therefore creating larger voids, consequently larger pore size. Figs 2e and f show SEM images of the PMM- and PS-based membrane, respectively after the final optimization of the chemical composition and electrospinning conditions. TEM images of single fibers are shown in the inset. The large diameter of the individual fibers also leads to increasing the thickness of the final membrane structure. Figs 2g and h show the measured thickness of the PMMA-and PS-based membranes of 43μm and 126 μm, respectively, which were spun for 24 hours. The PMMA-PVP nanofibrous membranes exhibit a superior capacity for Caco-2 cell attachment compared to the PS-PVP nanofibers. This superiority can be attributed to their smaller fiber diameter and membrane thickness, which closely resemble the extracellular matrix (ECM) structure. These features establish a microenvironment conducive to cell attachment and growth. Caco-2 cells display a preference for PMMA-PVP substrates with smaller nanofiber diameters due to the higher

surface area-to-volume ratio and a balanced hydrophobic/hydrophilic ratio, promoting enhanced cell adhesion and proliferation. This facilitates efficient nutrient and waste exchange under dynamic flow, crucial for supporting cell growth and viability. The biomimetic environment provided by the PMMA-PVP nanofibrous membranes, characterized by a fiber diameter of 727 nm, a thickness of approximately 20 μm, and a pore size of 4.5 μm, along with a viscosity of 3,323 mPa.s, effectively mimics the natural ECM found in tissues, thereby enhancing cellular activities. In contrast, the larger diameter PS-PVP nanofibers (1,200 nm) and 100 μm membrane thickness are considerably larger than the preferred dimensions for Caco-2 cells, impeding cell-substrate attachment.

3.2 Bulk and Surface properties of the electrospun membrane

Membrane wettability plays a crucial role in modulating cell attachment and differentiation. The wettability of the surface can be determined by measuring the contact angle between a droplet of water and a nanofibrous mat which consequently determine its hydrophilicity/hydrophobicity. When the contact angle is higher than 90 degrees, the surface is considered hydrophobic, while it is considered hydrophilic the contact angle is less than 90 degrees. Cell adhesion and proliferation are most effectively achieved between 35° and 80° of contact angle. Above or below this range will alter cell behavior [47]. It was found that adding PVP to PMMA or PS enhances the wettability of the electrospun (Fig. 3a). The measured static contact angles of the membranes fabricated using PMMA and PS (i.e., without PVP) were 91.5 ± 0.83° and 95.7 ± 0.84°, respectively, demonstrating the hydrophobic behavior of these porous structures without any chemical modification. A notable feature of PVP is its hydrophilic incorporation into non-wettable surfaces. Interestingly, this was sufficient to tune the surface wettability to attain moderate hydrophilicity in both membranes, which is favorable to improve cellular adhesion and differentiation as well enabling diffusion of

nutrients to cells. Adding PVP, with a ratio PMMA/PS:PVP of 5:1 significantly improved the wettability of both membranes. The measured contact angles of the membranes fabricated using PMMA-PVP and PS-PVP were 72.9 ± 0.6° and 82.60 ± 0.72°, respectively (Fig. 3a) which implies a reduction of contact angle by 21% and 14% compared to the reference samples. In fact, the presence of PVP and the functionalization of polymeric solutions with it increases the hydrophilicity of nanofibrous membranes, resulting in a decrease in the contact angle. This decrease in contact angle improves cellular adhesion, making the membrane better suited to biological applications.

Dynamic light scattering (DLS) is a useful verification tool for determining nanomaterial hydrodynamic size (DH) which also has been used to confirm the nanoscale dimensions for the nanofibrous mesh-like structures. The hydrodynamic size of the PMMA-based nanofibers was measured as 955.4 ± 41.5 nm with a polydispersity index (PdI) of 0.47 ± 0.16. On the other hand, the hydrodynamic size of the PS-based nanofibers was 1,281 ± 50 μm with a PdI of 0.81 ± 0.17 nm which are larger than those of the PMMA-based nanofibers (Fig.3b). During fiber formation, high tension is applied to the electrospinning jet, altering the PMMA polymeric chain orientation and reducing its PDI, which is usually close to 1 for high molecular weight polymers.

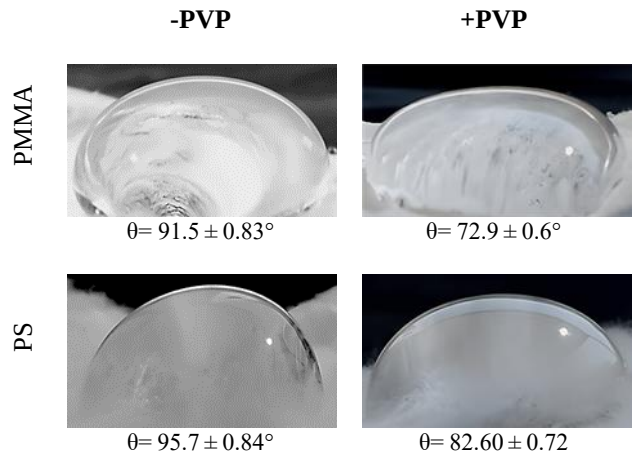

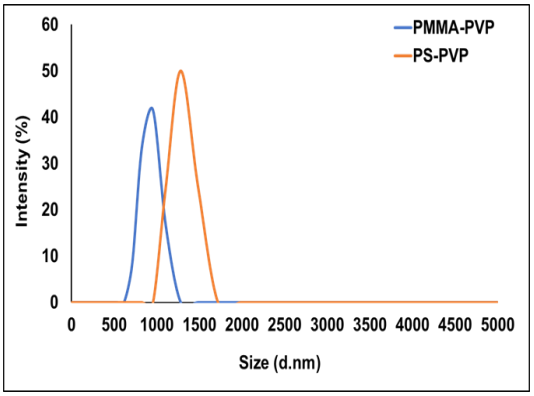

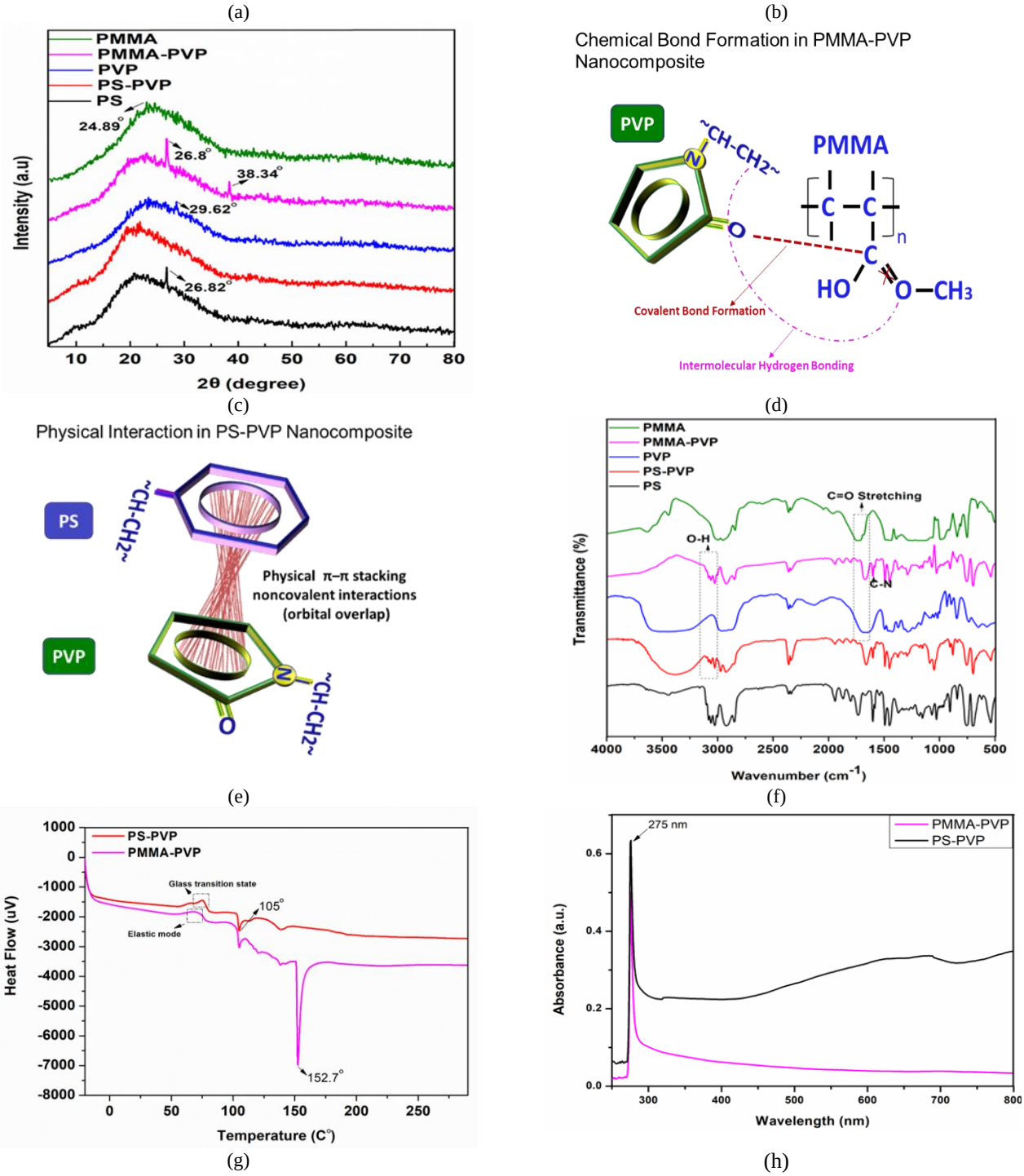

Figure 3: The measured contact angles of the electrospun membranes. Adding PVP to PMMA or PS enhances the wettability of the electrospun membrane. (b) The hydrodynamic size of the PMMA-and PS-based nanofibers was measured as 955.4 ± 41.5 nm and 1,281 ± 50 μm, respectively. (c) The XRD patterns of the PMMA, PMMA-PVP, PVP, PS-PVP, and PS electrospun nanofibrous membranes. (d) The intermolecular hydrogen bonds formed a flexible backbone in the polymeric complex's crystalline state, which induce a new bond peak in the mixture due to the incorporation of PVP with PMMA. (e) The disappearance of the PS polymer crystalline diffraction

peak along with the shifting of the broadened diffraction halo towards smaller diffraction angles is corresponding to the π-π stacking and overlap of aromatic and pyrrolidine rings among the polymers. (f) The FTIR spectra of PMMA, PMMA-PVP, PVP, PS-PVP, and PS. (g) The DSC results show exceptional stability of the nanocomposites even under high sterilization temperatures and dynamic microfluidic conditions for an extended period of time. (h) The optical absorption measurements of PMMA-PVP and PS-PVP composite nanofibers.

The PdI value of the PMMA-PVP nanofibers which is close to 0.2 resulted in monodispersed nanofibers which leads to a more homogeneous and uniform fiber network. The DLS measurements are comparable to those obtained by SEM with a larger diameter size due to diffusion within the fluid, which supports our analysis under fluidic conditions.

Surface charge is a key parameter that governs protein adsorption and cell adhesion and behaviour. In order to analyse the surface charge and chemical stability of nanostructures, zeta potentials were measured (Table 2). The zeta potential at pH ranges from 5.5 to 7.5 were +95.9 mV and +47.3 mV for PMMA-PVP and PS-PVP, respectively. The increase of the positive charges on the membrane surfaces maximizes its interaction with cells that bear a net negative charge by electrostatic attraction [48]. In fact, the electrophoretic effect of the charged nanofibers together with the dynamic fluid laminar flow strongly influence the interaction between cells and the polymeric membrane surfaces embedded in a microfluidic channel device, independently and cooperatively. Collectively, surfaces with highly positive charges promote adhesion and proliferation of cells. The PMMA-PVP nanofibrous membrane has a hydrodynamic diameter of hundreds of nanometers and a positive surface charge. This allows for the integration and proliferation of Caco-2 cells, leading to the development of a functional epithelial barrier. This is crucial for modelling the function of the epithelial barrier and for applications like drug delivery and tissue engineering.

XRD was used to investigate how PVP polymer inclusion affected PMMA and PS amorphous/crystallographic structures. Fig.3c shows the XRD patterns of the PMMA, PMMA-PVP, PVP, PS-PVP, and neat PS electrospun nanofibrous membranes. Due to the amorphous nature of PMMA nanofibers, pure PMMA showed a diffraction hump between 15° and 35° and a major low-intensity crystalline peak at 23.58°. An expansive diffraction halo at 25.6 degrees, followed by a weak, narrow diffraction peak at 29.62 degrees, on the XRD of pure PVP reveals a semi-crystalline structure. Upon composite integration, it was observed that the PMMA-PVP polymeric complex had two distinct crystal peaks, one at 26.78°, some of which referred to the main diffraction peak of PMMA, and another at 38.34° that was distinguishable to this composite. The pristine polymer XRD diffraction peaks changed by shifting to higher angle degrees with greater intensities. This was caused by strong covalent interaction between the ester-carbonyl groups in PMMA and the amide groups in PVP, which was consistent with the FTIR assessment. Furthermore, the intermolecular hydrogen bonds formed a flexible backbone in the polymeric complex's crystalline state, resulting in widened full-width half maxima (FWHM) of PMMA's major crystalline peaks and inducing a new bond peak in the mixture, which has been linked to the successful incorporation of PVP with PMMA (Fig.3d). This strong crosslinking and functionalization led the molecular chains to be ordered and entangled in crystalline regions rather than amorphous regions, increasing the polymer chains' stiffness; thus, the hybrid membrane revealed a better crystalline structure than pristine PVP and PMMA nanofibers. These results indicate that the degree of crystallinity increases as the flexibility and crosslinking density of the polymer chain increase PS nanofibers, on the other hand, revealed semicrystalline states, according to XRD patterns. These patterns demonstrated minor and wide humps at $2\theta = 9.68°$ and 23.34° and an extra high-intensity crystalline peak at $2\theta = 26.82°$. However, in the PS-PVP hybrid, the

disappearance of the PS polymer crystalline diffraction peak along with the shifting of the broadened diffraction halo towards smaller diffraction angles is corresponding to the π-π stacking and overlap of aromatic and pyrrolidine rings among the polymers (Fig.3e), which, influenced by the steric hindrance effect, leads to the polymer chains jumbling randomly with weak electrostatic interaction, thus hindering the crystallinity of the polymeric composite.

The FTIR spectra of PMMA, PMMA-PVP, PVP, PS-PVP, and PS are shown in Fig.3f. The C=O stretching band signals of the ester group in pristine PMMA and the amide group in pristine PVP were detected at 1733 cm-1and 1666 cm^{-1}, respectively. However, these prominent peaks after complex formation in PMMA-PVP nanocomposite were red-shifted to lower energy bands at 1672 cm-1 and 1600 cm^{-1}, respectively, with declining in energy peaks' intensities, indicating chemical bond formation between PMMA and PVP. A signal for C-N stretching vibrations of embedded PVP appears at 1288 cm^{-1} because the PVP chains are fixed within PMMA. Among the changes observed, O-H transitions were observed in the 3000–3100 cm^{-1} region due to intermolecular hydrogen bonds. In contrast, the broad absorption peak of PVP's pyrrolidone cyclic amide vanished from the 3495 cm^{-1} region compared to the pure PVP mats. In the PS-PVP nanocomposite, we observed IR peaks at 2860 cm^{-1} and 2928 cm^{-1}, which correspond to the vibrations of CH and CH2 groups in both PS and PVP. In the PS-PVP composite, two absorption peaks at 1495 and 1450 cm^{-1}were identified, which indicates the existence of phenyl ring of PS. The characteristic sharp peaks for PVP are visible at 1710 cm^{-1} and 1275 cm^{-1} for C=O and C–N groups, respectively, with a broad peak at 3417 cm^{-1} for the OH groups. These findings confirm the incorporation of PS with PVP in the nanocomposite in contrast to the pristine PS and pristine PVP.

XRD and FTIR analyses have confirmed the functionalization of nanofibrous membranes with PVP, resulting in a balanced hydrophobic-hydrophilic ratio that enhances cellular interactions with

the membrane and promotes adhesion and proliferation. The cross-linking between PMMA and PVP amplifies the membrane's crystallinity, improving its mechanical strength in consistency with DSC analysis. In addition, the OH and CO groups on nanofibrous membranes promote cellular attachment, creating a biomimetic ECM that supports cell proliferation and epithelium barrier generation. Conversely, the pi-pi stacking interactions between aromatic rings can impede cellular attachment on nanofibrous membranes, as evidenced by fewer Caco2 cells attached to the membrane as in the bright field images (Fig. 6b). These interactions yield fewer functional groups, potentially less conducive to cellular adhesion than surfaces with functional groups that promote cell attachment. Also, π interactions are linked to a reduction in diffusivity, which is not favorable for drug delivery applications.

Both fibrous substrates were shown to possess excellent mechanical properties. The Youngs modulus (Table 3) and material transition assessment (Fig. 3g), which are determined by pressure and temperature, show that PMMA-PVP is superior and more thermally stable and elastic (rubbery) than PS-PVP, likely due to the combined merits of synthetic polymers. The DSC results shown in Fig. 3e demonstrated the exceptional stability of the nanocomposites even under high sterilization temperatures and dynamic microfluidic conditions for extended periods. The PS-PVP curve obtained from the DSC graph highlights that this nanocomposite exhibits a remarkably higher glass transition state, which maintains its glassy and hard state until approximately 80 degrees. This is in accordance with the hardness analysis that shows 1.93 Mpa, proving that it is indeed higher than the PMMA-PVP. Conversely, the PMMA-PVP nanocomposite displays superior elastic properties, with a lower glass transition state than the PS-PVP. This is because the polymeric complex absorbs heat to become a more rubbery and elastic membrane, as confirmed by the Young's modulus analysis that shows the PMMA-PVP has 11.85 Mpa elasticity, which is

indeed higher than the PS-PVP nanocomposite studied by the non-indentation technique for mechanical property analysis. These results undoubtedly indicate that the PMMA-PVP is the preferable elastic cell culture membrane, which is more powerful under hydrodynamic conditions than the glassy, hard, and rough PS-PVP membrane. Thus, it is undoubtedly the preferable option for cell culturing.

Table 3: Young's modulus and hardness of the electrospun nanofibers

Nanofibers	Young's Modulus (Mpa)	Hardness (Mpa)
PMMA-PVP	11.85	1.04
PS-PVP	11	1.93

The optical absorption characteristics of the nanofibers may be altered by varying the coupling polymer and its concentration [49, 50], such as PVP in our study. PVP crosslinking to PMMA and PS also influences the linear optical properties, such as the band gap associated with absorbance. The optical absorption measurements of PMMA-PVP and PS-PVP composite nanofibers have been carried out as shown in Fig. 3h. All nanofiber composites' PVP absorbance UV-Vis spectra were blue shifted from 330 nm to 275 nm, which confirms that PVP is embedded into the polymer matrixes. In addition, the absorbance edges follow a sharp increase, indicating that the nanofibers have a crystalline structure. In consistency to SEM observations, the expansion in the UV absorption intensity region of PS-PVP composite suggests band gap tenability and is attributable to the increase in light-scattering intensity owing to the increase in membrane thickness. As the thickness of the membrane increases, the transmittance of light declines significantly [51]. In summary, the PMMA-PVP membrane exhibits a thinner profile in comparison to the PS-PVP membrane. This characteristic enhances drug diffusivity and permeability, thereby effectively

facilitating the absorption and transportation of drugs. Consequently, the PMMA-PVP membrane serves as a suitable substrate for the biofabrication of epithelial layers.

3.3. Fabrication and integration of the fiber-based PM

A key enabling feature of our fabricated device and method is the ability of direct deposition (in situ) and integration of the PM into the microfluidic chip which eliminates lengthy assembly process. The direct deposition of the membrane onto a patterned polymer (PMMA or PS) layer (i.e., with the fluidic structures are cut out) has shown firm attachment of the membrane onto the polymer surface. This is evident from the fact that the device can withstand fluidic testing at different flow rates, ranging from low to high (e.g., 1-200 μL/min), without any fluid leakage. Furthermore, our fabrication methodology allows the deposition of the fibers onto a large surface with multi-compartment structure. This allows for the parallel integration of the membrane onto a large number of chips. The PM was electrospun using two polymers (i.e., PMMA and PS) as explained in section 2.2. The PMMA and PS fiber membranes were fabricated and integrated into three chips with different designs: (a) fam1: comprises one basolateral chamber and one apical chamber sandwiching a PM (PMMA or PS) (Fig. 4a); (b) fam2: comprises one basolateral chamber and two apical chambers both overlapping the basolateral chamber through the PM (Fig.4b); fam4: Comprises three basolateral chambers and four apical chambers overlapping through the PM. The middle basolateral chamber overlaps with two apical chambers similar to fam2 (Fig. 4c). Figs.4a, 4b, and 4c show the designed, fabricated and flow-tested chips for fam1, fam2, and fam4 chips, respectively. The results demonstrated the feasibility of direct deposition of the fiber-based membrane onto patterned surfaces with simple (Fig. 4a) and complex (Figs 4b and 4c) patterns. Both the PMMA- and PS-based withstood the pressure imposed by the fluid flow up to a flow rate of 200 μL/min. Coloured water was used to enable better visualization.

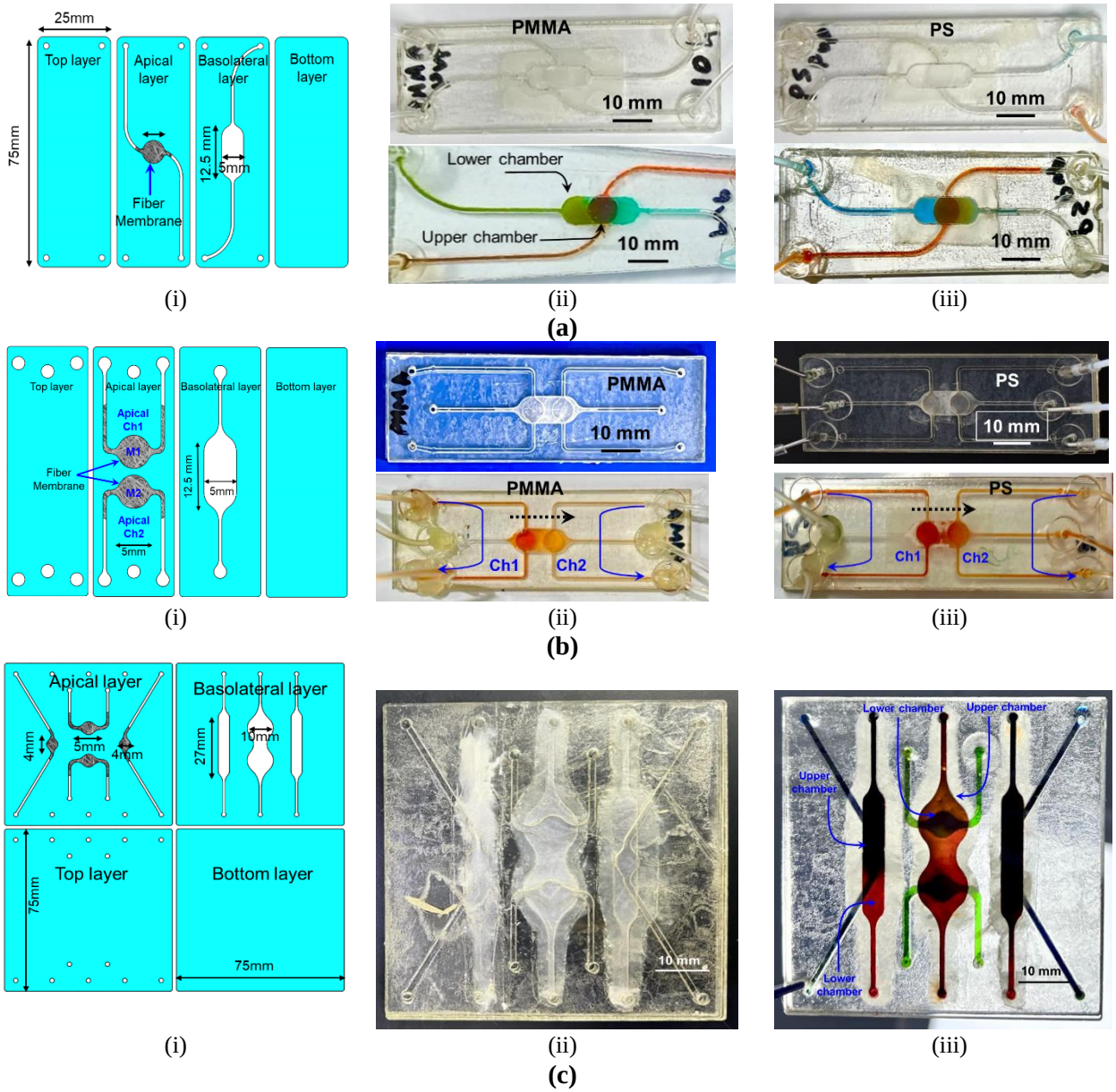

Figure 4: Preliminary test of the PMMA and PS fiber-based membranes after assembly. (a) The *fam1* chip comprises one basolateral chamber and one apical chamber sandwiching a PM (PMMA or PS). i) The designed four layers which form the chip; ii) The assembled chip (top) with PMMA-based membrane and the tested chip (down); iii) The assembled chip (top) with PS-based membrane and the tested chip (down). (b) The *fam2* chip comprises one basolateral chamber and two apical chambers both overlapping the basolateral chamber through the PM. sandwiching a PM (PMMA or PS). i) The designed four layers which form the chip showing the fiber-based PM deposited onto the basolateral layer, ii) The assembled chip (top) with PMMA-based membrane and the tested chip (down); iii) The assembled chip (top) with PS-based membrane and the tested chip (down). (c) The *fam4* chip comprises three basolateral chambers and four apical chambers overlapping through the PM. i) The designed four layers which form the chip; ii) The assembled chip with a PMMA-based membrane; iii) the tested chip.

3.4 Thickness, porosity, and permeability analysis

Porous membranes play a crucial role in cell culture by enabling the partitioning of cellular microenvironments in vitro while allowing physical and biochemical crosstalk between cells. These membranes serve as essential tools for studying cell behaviour in a controlled environment, including the creation of barriers that separate distinct cell populations within a culture system. Moreover, they enable mimicking of the natural tissue barriers, such as the intestinal epithelium, and they are instrumental in studying cell migration and drug testing. The morphology and porosity of the membrane have a significant impact on cell culture and cellular crosstalk. The specific characteristics of the membrane, such as its pore size, shape, and distribution, can influence the behaviour and interactions of cells within the culture system. The porosity of the membrane determines the ability of cells to migrate and communicate with each other. A membrane with larger pores allows for increased cell migration and exchange of molecules, facilitating cellular crosstalk. On the other hand, a membrane with smaller pores restricts cell movement and limits the diffusion of molecules, leading to more localized cellular interactions. Additionally, the morphology of the membrane, including its surface topography and structure, can affect cell adhesion, proliferation, and differentiation. A membrane with a smooth surface promotes cell attachment and growth, while a textured or patterned surface can guide cell alignment and organization [52]. Unlike the track etched porous membranes, the thickness of the fiber-based membrane significantly influences its porosity. A thicker membrane provides more materials due to the stacking of multilayers of fibers that form solid walls between the pores restricting the available pore space. On the other hand, a thinner membrane has a higher porosity as there is less material obstructing the pores. This allows for a greater volume of interconnected voids, enabling the passage of fluids and molecules through the membrane. Various membranes with different

thicknesses were fabricated on the chip FAM 1 by varying the electrospinning times. Longer electrospinning times resulted in thicker membranes. SEM images in Figs 5a and b depict the variations in membrane thickness for PMMA-PVP and PS-PVP, respectively. For the PMMA-based membrane, a thickness of 62 μm was achieved with a two-hour electrospinning time. The thickness increased to 736 μm after twelve hours. On the other hand, the PS-based membrane exhibited a larger single fiber diameter, leading to much thicker membranes at the same electrospinning periods (Fig. 5b). A two-hour spinning time produced a 517 μm thick membrane, while a twelve-hour spinning time resulted in a thickness of 2488 μm. Fig. 5c provides a summary of these results for both PMMA and PS-based membranes, demonstrating that the spinning rates are not linear. To obtain an optimum permeable membrane for a specific application, the thickness must be optimized based on the desired porosity and permeability. By considering the chemical composition, material properties and electrospinning conditions, membranes can be tailored to achieve the desired thickness and porosity. The permeability of membranes was evaluated by injecting FITC-Dextran (40 KDa) with a concentration of 10 μg/ml into the upper (apical) chamber and collecting the perfusate from lower (basolateral) chamber at an injection flow rate of 1 μl/min. The perfusate samples were collected at different time intervals, and the fluorescence intensity (FI) was measured which is correlated to the membrane permeability. Figs 5d and e show that FITC intensity steadily increases with increasing the time for an individual membrane through 24 h which indicates a steady mass transfer and cross-compartment communication. Also, the permeability drastically decreases when the membrane thickness increases for both PMMA and PS-based membrane (Figs 5d and e). Due to the higher thickness of the PS membranes, they became less permeable (Fig. 5e). The permeability of the PMMA-based membrane with thickness of 62μm is comparable to that of a commercial track etched membrane with thickness of 10 μm

and pores size of 0.4 µm (Fig. 5f). These results demonstrate the usability and modularity of the nanofiber-based membranes as permeable substrates for epithelial cell culture as tissue barriers.

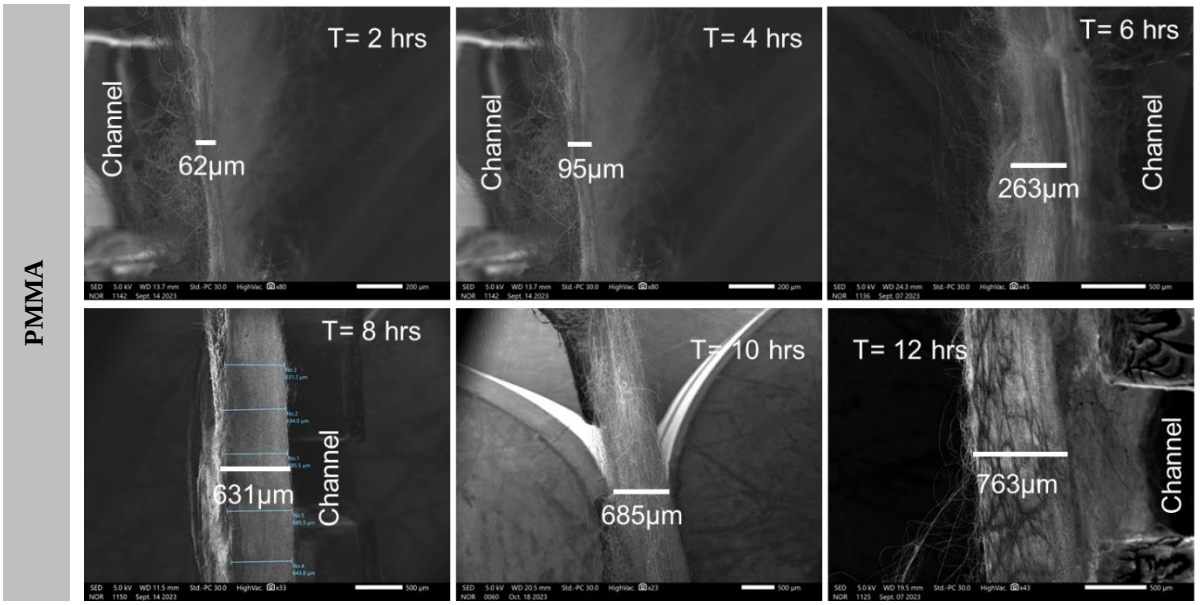

(a)

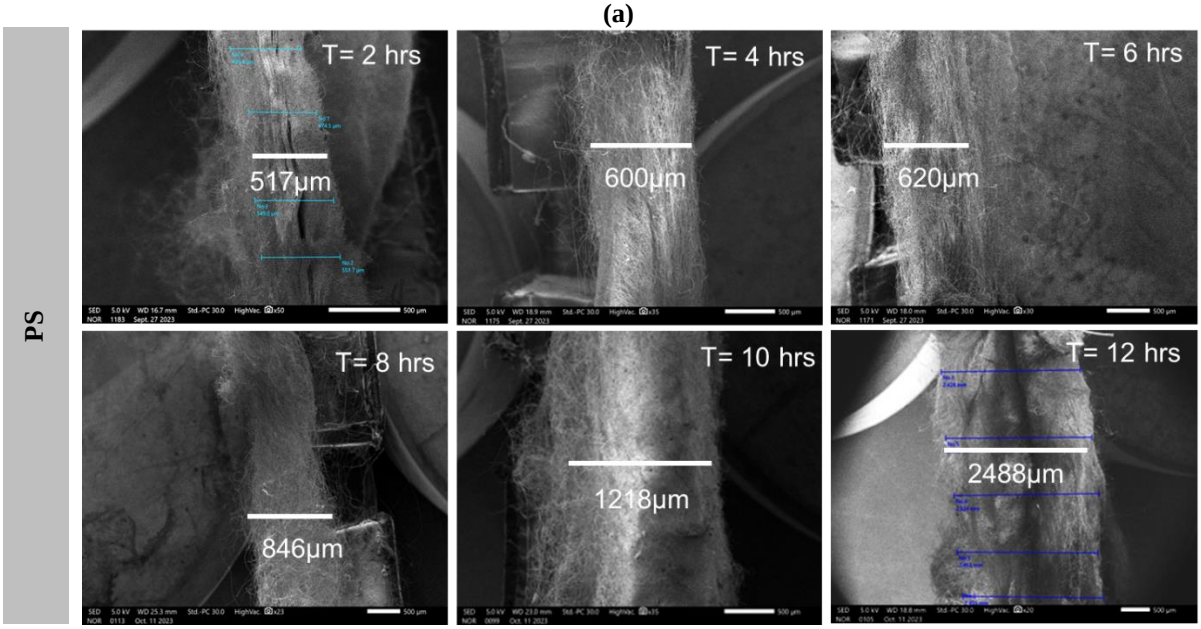

(b)

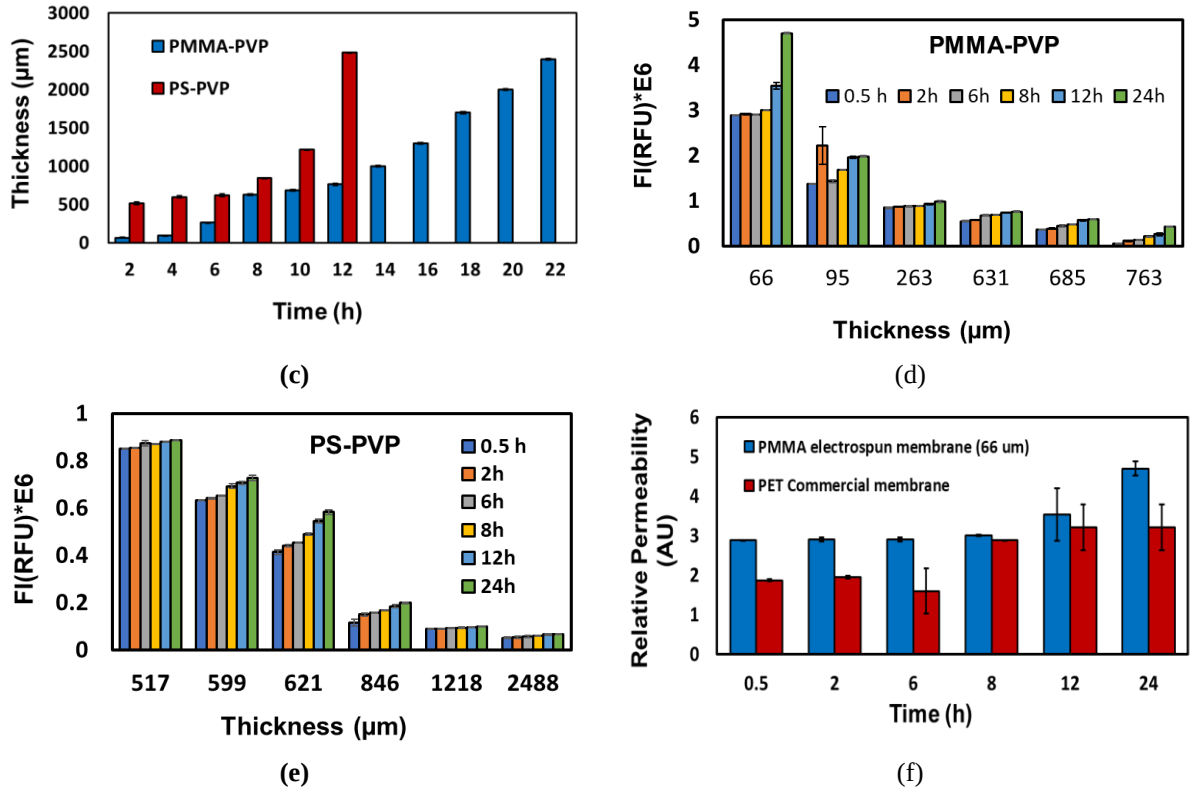

Figure 5: (a-b) SEM images that show various electrospun membranes with different thicknesses for PMMA-PVP and PS-PVP, respectively obtained at different electrospinning timing. Thicker membranes were obtained by elongating the spinning periods. (c) Summary of the results obtained by the SEM images in a and b. (d-e) The permeability of FITC-Dextran (4 KDa) through the membranes with different thicknesses. The fluorescence intensity of the perfusate was measured and correlated to the membrane permeability. As expected, the permeability drastically decreases with increasing of the membrane thickness. (f) The permeability of the PMMA-based membrane with thickness of 62µm is comparable to that of a commercial etched membrane with thickness of 10 µm and pores size of 0.4 µm.

3.5 Constructing an intestinal epithelial barrier model on the fiber-based membrane

Caco-2 cells were cultivated on the fam2 chip in two configurations: either on one membrane, M1 (Fig. 1f), or on two membranes, M1 and M2 (Fig. 1g). This setup aimed to demonstrate the feasibility of creating two tissue barriers on a single chip. In this study, one cell line is used for this purpose. Prior to seeding, the chip was sterilized, and the membrane was coated with collagen I, and the chip was connected to the perfusion circuit (Figs 1e) at a flow rate of 1 µL/min. Figs 6a and b show the attachment and proliferation of cells on the PMM-based and PS-based membrane,

respectively, over a two-week culture period. It was observed that cell attachment and proliferation were generally more favourable on the PMMA-based membrane (Fig. 6a) compared to the PS-based membrane (Fig. 6b). A fully confluent cell monolayer was established after ~8-10 days of culture on top of the PMMA membrane compared to 14 days on top of the PS membrane (Fig. 6b). Fig. 6c shows a series of SEM images of the fully confluent monolayer at different magnifications. The images show continuous tissue layer (top panel) and clear cell borders or the gap between the cells at higher magnification (bottom panel). The cell attachment onto the membrane's fibers is clearly shown in Fig. 6d with an estimated height of the cell monolayer of ~20 μm. The PMMA fibers exhibited a conducive environment for rapid cell attachment. The cells at 10 days of culture became fully differentiated columnar enterocytes as evidenced by presence of the microvilli structure on the apical side of the cells as well as the tight junction's proteins in the intracellular borders (Fig.6e). These are two key characteristics of the fully differentiated absorptive enterocytes located in the villi of the small intestine, hence can serve as a good model for studying the para– and trans-cellular transport through the human small intestine. Furthermore, it was observed that topography of the epithelial monolayer grown on the fiber-based membrane is not flat but is characterized by many hump-shaped structures with estimated height of 100-200 μm (Fig. 6f). It is important to recognize that the small intestine possesses a distinctive structure characterized by the presence of finger-like protrusions known as villi which play a vital role in the absorption of nutrients. It was found that the cells exhibited clear columnar morphology when cultured on a membrane with dense nanofiber-membrane (i.e., with a small resultant pore size) compared to those cultured on a less density nanofiber membrane. Therefore, it's important to recognize the significant impact of a porous substrate and the dynamic environment created by fluid flow on both the apical and basolateral chambers. This dynamic flow enhances and

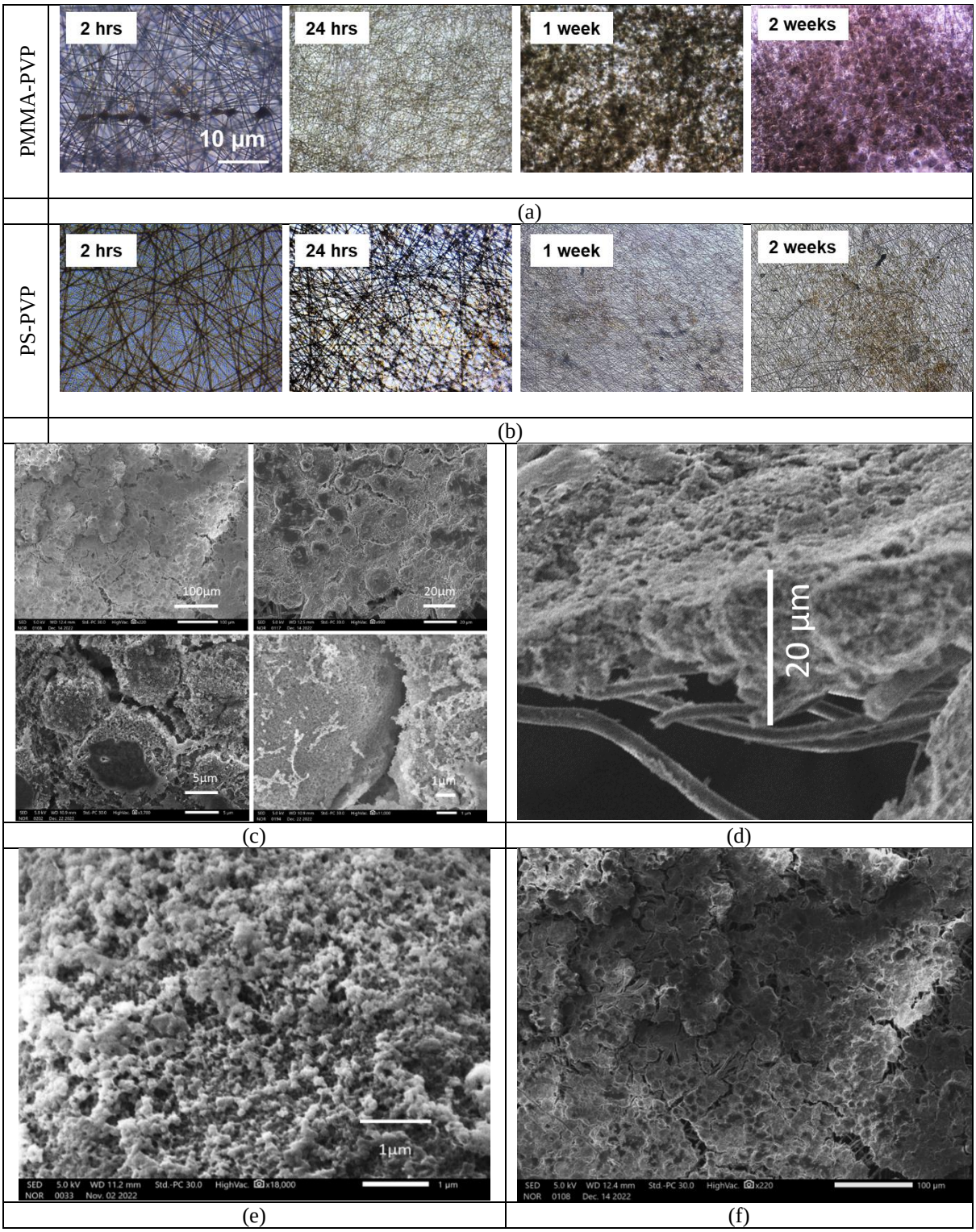
PMMA-PVP
2 hrs
24 hrs
1 week
2 weeks
10 µm
(a)
PS-PVP
2 hrs
24 hrs
1 week
2 weeks
(b)
100µm
20µm
5µm
1µm
(c)
20 µm
(d)
1µm
(e)
100 µm
(f)

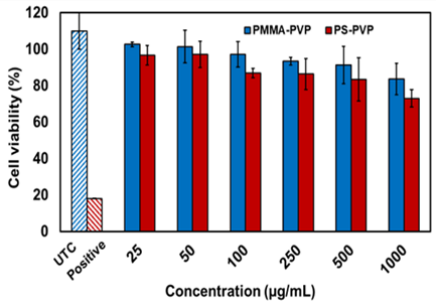

(g)

Figure 6: (a) Cell growth profile on the PMMA membrane for 2 weeks. (b) Cell growth profile on the PMMA membrane for 2 weeks. Fully confluent monolayers of caco-2 cells were formed on both membranes within the two weesk of culture. (c) A series of SEM images of the confluent monolayer on the PMMA membrane. The iamaging was conducted after 21 days of culture. (d) Cross-sectional view showing the cell attachment on the fibesr. The estimated height of the monolayer is ~20 µm. (e) Microvilli structure was established on the apical side of the cells which indicates the differentation of the cells to apsorbative eneterocytes. (f) The morphology of the cell monolayer appears rough with many hump-shaped structures. (g) The biocompatibility, expressed as cell viability percentage, of both membranes was evaluated over a 48-hour period using different concentrations of deposited electrospun nanofiber membranes..

accelerates the polarization and differentiation processes of the Caco-2 cells. Therefore, it worths to note that the presence of a porous substrate and the dynamic environment provided by the fluid flow across both the apical and the basolateral chambers (i.e., above and under the cells/membrane) would enhance and accelerate the polarization and differentiation processes of the caco-2 cells [53]. The epithelial cells in the small intestine have columnar morphology [54]. Therefore, our membrane chip which provides a porous substrate and dynamic flow is able to imitate the in vivo morphology of these cells. These findings are supported by the SEM images shown in Fig. 6.

The nanofiber-based membrane has been developed and integrated into a cell culture chip aiming to conduct long-term experiments. It is crucial to ensure that cells can survive on this membrane without experiencing any cytotoxic effects. In order to investigate cell viability, caco-2 cells were treated with various concentrations of both PMMA-PVP and PS-PVP nanofibers. The results, as depicted in Fig.6g, indicate that both types of fibers exhibit negligible cytotoxic effects. The biocompatibility of the nanofibrous membranes was evaluated by comparing the number of viable

cells treated with the nanofibers to the number of viable cells in the untreated control and positive control groups using the Alamar blue assay. There is a clear temporal proliferation profile of the cells after 48 hours of culture on both membranes, showing high biocompatibility at the concentration of 100 μg/mL, which is the calculated concentration of the nanofiber mat that will be deposited on the chip within the specified dimensions, as previously explained. Notably, all of the samples exhibited viable cells. However, the cell viability on the PMMA-PVP membranes was significantly higher than that of the PS-PVP nanofibers at 1000 μg/mL (cell viability % > 70). These rsults indicates that PMMA mats offer greater biocompatibility for long-term bio experiments (Fig. 6.g). These results suggest that the polymeric composite membranes contribute to cell proliferation. This is likely due to the increased presence of oxygen-containing groups, such as carbonyl and carboxyl, in polymeric composites, as confirmed by FTIR analysis. To promote cell adhesion, the PMMA and PS surfaces were functionalized with PVP to introduce biologically relevant chemistry, such as carbonyl and amine groups. It should be noted that the pure PMMA and PS nanofibers were not subjected to cytotoxicity studies due to their hydrophobic nature, which prevented the penetration of cell culture media. Additionally, pure PVP was not stable under dynamic flow experiments as it dissolved in the media due to its high hydrophilicity.

3.6 Functional characterization of the intestinal epithelial barrier model

In order to effectively utilize the developed in vitro model of the intestinal barrier for permeability assays, it is crucial that the model meets the key structural criteria observed in vivo. This includes the presence of a fully confluent monolayer of differentiated enterocytes that express paracellular tight junctions (TJs) and microvilli. To evaluate the integrity of the barrier, the device is integrated with four electrodes (Fig. 1a) for measuring the TEER across the cell layer which can

also be correlated to the permeability of the barrier. Fig.7a shows the TEER data obtained during twelve days of culture. TEER value significantly increased after one week, which indicates the TJ formation. The TJ formation has also been confirmed with immunofluorescence staining by visualizing the expression of TJ protein occludin as shown in Fig. 7b.

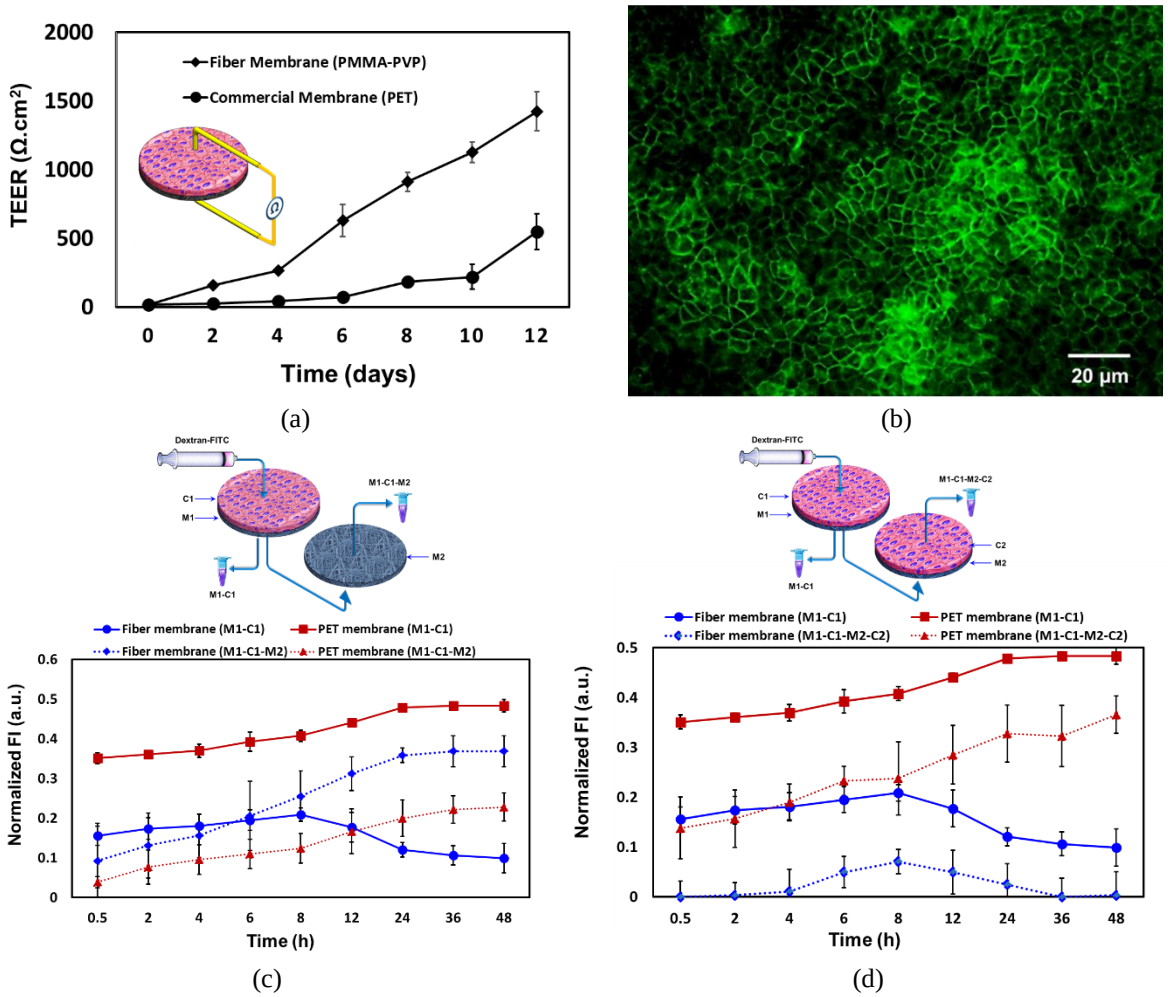

Figure 7: (a) TEER measurements of caco-2 cell monolayer taken over twelve days. Cells were grown on two chips, one with a fiber-based membrane and the one with a commercial PET membrane. (b) TJ formed by adjacent Caco-2. The TJs were stained by FITC-labelled anti-mouse occluding. Images of confluent monolayer formed by Caco-2 cells taken on the day 14 under 10× objective lens. (c) The FITC-dextran permeability through a single cell monolayer and two membranes. Cells were grown on chips with fiber-based membrane and PET membrane. (d) The FITC-dextran permeability through two cell monolayers and two membranes. Cells were grown on chips with fiber-based membrane and PET membrane.

Subsequently, the permeability of FITC-dextran (40 kDa) was studied in two cellular systems (i.e., one epithelial monolayer and two epithelial monolayers) (Figs 1f and g). As shown in Figs 7b and d, the permeability of the cell monolayer grown on the fiber-based membrane is found to be significantly lower than that of the cells grown on the PET membrane. These results are supported by the TEER measurements shown in Fig. 7a. Indeed, the observed reduction in permeability of the epithelial monolayer is directly associated with its integrity. A well-functioning barrier is essential for effectively protecting tissues, regulating transport processes, and preventing the entry of harmful substances. A disturbed barrier function has been linked to several chronic conditions which originate in the gastrointestinal tract [55, 56]. Fig. 7d shows the permeability of the indicator transporting through two epithelial monolayers, where the indictor molecules permeate the first monolayer through the apical-to-basolateral rout then permeate the second monolayer through the basolateral-to-apical rout (Fig. 7d inset). Notably, the second monolayer significantly reduces the permeability of the indicator which demonstrates the functionality of the in vitro model of the barrier. It should be noted that the cell monolayer arrangement shown in Fig. 7d may not precisely replicate the anatomical structure of an in vivo system. However, the purpose of this arrangement is to showcase the feasibility of tracking crosstalk in a complex and compartmentalized cellular system.

The efficacy of the system for oral drug absorption was assessed by validating the transport of an active molecule across the caco-2 monolayer using metformin. Metformin is a first-line therapy for type 2 diabetes mellitus used to reduce blood glucose levels and is one of the most commonly prescribed drugs worldwide. It is rapidly absorbed in the small intestine, with negligible absorption in the stomach or large intestine, [57] and does not bind to plasma proteins [58]. The first dose of metformin was administered by injecting a concentration of 100 μg/mL, which was diluted in the

culture media. The basolateral supernatant was then collected at various time intervals to assess the transport of metformin across the caco-2 monolayer. Another dose of metformin with the same concentration was applied after 11 hours. The subsequent basolateral supernatant was collected at additional time intervals to continue monitoring the transport of metformin. Fig. 8 shows the transported amount of 65±0.523 µg and 64.5±0.0001 µg after 0.5h and 2h, respectively. The transported amount dropped to 32±0.179 after 8h. One hour after applying the second dose, the transported amount reached 44±1.3 µg and continued to decline reaching 32±0.35 µg after 48 h. The calculated apparent permeability coefficients (Papp) from the cumulative permeability data ranged from 5.6×10^{-6} cm/s to 11.5×10^{-6} cm/s. The Apical-to-basolateral transport of metformin is correlated with the applied dose in the apical compartment. The drug molecule permeated through the monolayer at a varying rate at two different doses through the experiments without damaging the monolayer. The permeability profiles of dextran (Fig.7c and d) and metformin (Fig. 8) confirm the ability of the caco-2 monolayer, which was grown on the nanofiber membrane, to study the transport of macromolecules and small molecules across the intestinal epithelium. Drug molecules may transport through the intestinal epithelium via different pathways depending on their size and hydrophilicity. Large molecules such as dextran (40kDa) and metformin (165 kDa) may not permeate through the paracellular route due to their size and hydrophilic nature [59, 60]. At physiological pHs, metformin is a hydrophilic cation which is highly soluble but poorly permeable in the intestine [61, 62]. The oral absorption of metformin in humans is dose-dependent and saturable, indicating the involvement of a complex transport-mediated mechanism [63]. This in vitro model can be aptly used to study the different permeation pathways of small and macromolecules through the intestinal epithelium and identify methods for enhancing the absorption of drug candidates. In addition, it is evident that the PMMA-PVP membrane exhibits a

notably high light transmittance. This characteristic implies minimal interaction with drugs and high permeability, thereby endowing it with significant value for drug delivery application studies.

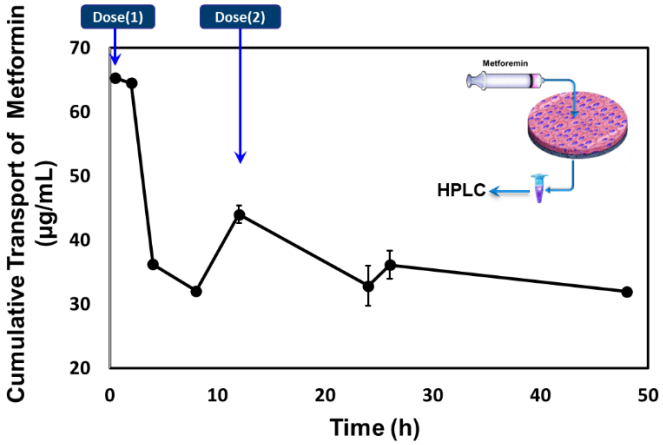

Figure 8: Time-course study of apical-basolateral dynamic transport of metformin. The metformin solution was loaded in the apical compartment at 100µg/mL and the permeation was measured in the basolateral supernatant using HPLC. Data represent mean±SD (n = 3).

3.7 General Discussions

Integrating the porous membrane into the streamline of cell culture device fabrication eliminates the need for additional assembly steps, minimizing the risk of errors and enhancing efficiency. This simplification of the fabrication enables easier scaling up of the fabrication process which is crucial for potential industrial applications where high-volume production is necessary. In fact, the membrane becomes an essential part of the device design, facilitating mass production without compromising quality or functionality. Additionally, by designing the device with the membrane, it allows for optimal alignment, proper attachment, and improved stability, consistency and reproducibility of the membrane within the device structure which ensures that the membrane functions as intended, providing the desired permeability, porosity, and mechanical properties.

The chemical composition and rheological properties of the polymer, including polymer concentration, molecular weight, viscosity, and solvent choice, play a crucial role in shaping the

resulting fiber and membrane morphology. Factors such as diameter, alignment, and overall structure of the fibers are influenced by these properties. Furthermore, the electrospinning conditions, such as voltage, flow rate, and distance between the spinneret and collector, also contribute to morphology. Understanding and controlling these parameters is pivotal for achieving the desired fiber and membrane characteristics. The electrospun membrane exhibits distinctive bulk and surface properties which were investigated in this study. The surface properties, such as roughness, hydrophilicity, and surface charge, play a crucial role in cell adhesion, proliferation, and overall biocompatibility. The bulk properties include mechanical strength, flexibility, and thermal stability, which are essential for the membrane's functionality and durability. Analyzing and characterizing these properties are important for assessing the suitability of integrating the membrane into the cell culture devices and drug screening applications. The resultant thickness of the membrane can be tailored to optimize the mechanical strength, flexibility and porosity. Porosity influences the diffusion of gases, nutrients, and waste products as well cell-cell crosstalk in co-culture systems which are vital for mimicking physiological conditions. The processes and results described in this study demonstrated the suitability of the in-situ electrospinning to provide a microfluidic platform for constructing an in vitro model of tissue barrier (i.e., an intestinal epithelial barrier model). The structure and function of the constructed model were characterized to assess its ability to mimic the key features of the intestinal epithelium. This includes evaluating cell viability, proliferation, differentiation, and the expression of specific markers associated with the cell differentiation. The barrier integrity and paracellular transport across the barrier were assessed using a well-known oral drug (metformin) to determine its suitability for drug screening applications. Future study involves applying the developed process and platform for larger and more complex organ-on-a-chip devices for studying cell-cell crosstalk and disease modelling. By

incorporating the membrane, it becomes feasible to connect different organ models together, mimicking the interplay between organs in the human body. This allows for the study of systemic effects and the evaluation of how diseases or drug treatments affect multiple organs simultaneously, providing a more comprehensive understanding of complex physiological processes.

4. Conclusions

In this study, we successfully integrated a fiber-based porous membrane into the fabrication process of a 3D microfluidic device by directly depositing the fibers onto patterned surfaces with both simple and complex patterns. We carefully examined the bulk and surface properties of the membrane's fibers through a comprehensive analysis which includes the chemical composition of the polymers, the electrospinning process, and the structure and morphology of the fabricated membranes. We focused our investigation on two polymers: PMMA-PVP and PS-PVP to identify the polymer with the best performance for cell culture and drug transport applications. Our results showed that the PMMA-based membrane, specifically with a PMMA:PVP ratio of 5:1, allowed for the fabrication of a uniform membrane structure along the aligned nanofibers. Additionally, the diameter of the nanofibers in the PMMA-PVP mesh-like membrane was smaller compared to those in the PS-based membrane. The membrane porosity could be adjusted by modulating the fiber diameter and the total thickness of the membrane. During the fiber formation process, high tension is applied to the electrospinning jet, which altered the orientation of the PMMA polymeric chains and reduced its Polydispersity Index (PDI). Typically, high molecular weight polymers have a PDI close to 1, but the PMMA-PVP nanofibers exhibited a PDI value close to 0.2 which resulted in monodispersed nanofibers and a more homogeneous and uniform fiber network. Both types of membranes demonstrated excellent mechanical integrity under medium perfusion flow

rates of up to 200 µL/min. However, the PMMA-PVP composition offered a tailored porous structure with modulable porosity based on fiber diameter and thickness. This unique feature allowed us to develop a microfluidic chip with a custom porous substrate and dynamic flow, enabling dynamic culture of epithelial cells on the porous membrane. Our developed platform enables dynamic in vitro modelling of the epithelial barrier and has applications in drug transport and in vitro microphysiological systems and shows promise as a key component in the organ-on-a-chip devices.

AUTHOR INFORMATION

Corresponding Author

* qalramadan@alfaisal.edu; mzourob@alfaisal.edu

Author Contributions

The manuscript was written through contributions of all authors. All authors have given approval to the final version of the manuscript.

here). Follow the journal's guidelines on what to include in the Acknowledgments section.

ACKNOWLEDGMENTS

This work was conducted with the financial support of Alfaisal University under grant number 1274.

REFERENCES

[1]. Langer R.;Vacanti JP. Tissue engineering Science 1993, 14, 920-926.

[2]. Khademhosseini A.; Langer R.; Borenstein J.; Vacanti JP.; Microscale technologies for tissue engineering and biology Proc. Natl. Acad. Sci. U S A 2006, 21, 2480-2487.

[3]. Nadine S.; Chung A, Diltemiz SE.; Yasuda B.; Lee C.; Hosseini V.; Karamikamkar S.; de Barros NR.; Mandal K.; Advani S.; Zamanian BB.; Mecwan M.; Zhu Y.; Mofidfar M.; Zare MR.;

Mano J.; Dokmeci MR.; Alambeigi F.; Ahadian S. Advances in microfabrication technologies in tissue engineering and regenerative medicine. Artif. Organs 2022, 29, 211-243.

[4]. Ramadan Q.; Zourob M. Organ-on-a-chip engineering: Toward bridging the gap between lab and industry Biomicrofluidics 2020,14, 041501.

[5]. Chung HH.; Mireles M, Kwarta BJ.; Gaborski TR. Use of porous membranes in tissue barrier and co-culture models. Lab Chip 2018, 12, 1671-1689.

[6]. Kim HJ.; Huh D.; Hamilton G.; Ingber DE. Human gut-on-a-chip inhabited by microbial flora that experiences intestinal peristalsis-like motions and flow. Lab Chip. 2012, 12, 2165-2174.

[7]. Shin W.; Hinojosa CD.; Ingber DE.; Kim HJ. Human Intestinal Morphogenesis Controlled by Transepithelial Morphogen Gradient and Flow-Dependent Physical Cues in a Microengineered Gut-on-a-Chip iScience 2019, 31, 391-406.

[8]. Huang C.; Ramadan Q.; Wacker J. B.; Tekin, H. C.; Ruffert, C.; Vergères G.; Silacci P.; Gijs M. A. M.; Microfluidic chip for monitoring Ca2+ transport through a confluent layer of intestinal cells RSC Adv 2014, 4, 52887-52891.

[9]. Huh D.; Matthews BD.; Mammoto A.; Montoya-Zavala M.; Hsin HY.; Ingber DE.; Reconstituting organ-level lung functions on a chip Science 2010, 25, 1662-1668.

[10]. Achberger K.; Probst C.; Haderspeck J.; Bolz S.; Rogal J.; Chuchuy J.; Nikolova M.; Cora V.; Antkowiak L.; Haq W.; Shen N.; Schenke-Layland K.; Ueffing M.; Liebau S.; Loskill P. Merging organoid and organ-on-a-chip technology to generate complex multi-layer tissue models in a human retina-on-a-chip platform Elife 2019, 8, 46188.

[11]. Ramadan Q.; Ting FC. In vitro micro-physiological immune-competent model of the human skin. Lab Chip 2016, 16, 1899-908.

[12]. Chung HH.; Chan CK.; Khire TS.; Marsh GA.; Clark A Jr.; Waugh RE.; McGrath JL. Highly permeable silicon membranes for shear free chemotaxis and rapid cell labeling. Lab Chip 2014, 14, 2456-2468.

[13]. Wang Z.; Kim MC.; Marquez M.; Thorsen T. High-density microfluidic arrays for cell cytotoxicity analysis Lab Chip 2007,7, 740-745.

[14]. VanDersarl JJ.; Xu AM.; Melosh NA.; Rapid spatial and temporal controlled signal delivery over large cell culture areas Lab Chip 2011, 11, 3057-3063.

[15]. Loskill P.; Sezhian T.; Tharp KM.; Lee-Montiel FT.; Jeeawoody S.; Reese WM.; Zushin PH.; Stahl A.; Healy KE. WAT-on-a-chip: a physiologically relevant microfluidic system incorporating white adipose tissue Lab Chip 2017, 17, 1645-1654.

[16]. Ross AM.; Jiang Z.; Bastmeyer M.; Lahann J. Physical aspects of cell culture substrates: topography, roughness, and elasticity. Small 2012, 8, 336-55.

[17]. Sajay BNG.; Yin, C.; & Ramadan, Q. Optimization of micro-fabricated porous membranes for intestinal epithelial cell culture and in vitro modeling of the human intestinal barrier J. Micromech. Microeng. 2017, 27, 1361-6439.

[18]. Carter RN.; Casillo SM.; Mazzocchi AR.; DesOrmeaux JS.; Roussie JA.; Gaborski TR. Ultrathin transparent membranes for cellular barrier and co-culture models Biofabrication 2017, 9, 015019.

[19]. Ma SH.; Lepak LA.; Hussain RJ.; William S.; Shuler ML.; An endothelial and astrocyte co-culture model of the blood–brain barrier utilizing an ultra-thin, nanofabricated silicon nitride membrane Lab Chip2005,5, 74-85.

[20]. Tang B.; Bendas S.; Krajka V.; May T.; Moritz A.; Constantinou L.; Reichl S.; Dietzel A. Self-loading microfluidic platform with ultra-thin nanoporous membrane for organ-on-chip by wafer-level processing Front. Sens. 2022, 3, 2673-5067.

[21]. Kim MY.; Li DJ.; Pham LK.; Wong BG.; Hui EE. Microfabrication of High-Resolution Porous Membranes for Cell Culture J Memb Sci. 2014, 15, 460-469.

[22]. Musah S.; Mammoto A.; Ferrante TC.; Jeanty SSF.; Hirano-Kobayashi M.; Mammoto T.; Roberts K.; Chung S.; Novak R.; Ingram M.; Fatanat-Didar T.; Koshy S.; Weaver JC.; Church GM.; Ingber DE. Mature induced-pluripotent-stem-cell-derived human podocytes reconstitute kidney glomerular-capillary-wall function on a chip. Nat Biomed Eng. 2017, 1, 0069.

[23]. Vandenhaute E.; Drolez A.; Sevin E.; Gosselet F.; Mysiorek C.; Dehouck MP. Adapting coculture in vitro models of the blood-brain barrier for use in cancer research: maintaining an appropriate endothelial monolayer for the assessment of transendothelial migration Lab Invest. 2016, 96, 588-98.

[24]. Abu-Dawas S.; Alawami H.; Zourob M.; Ramadan Q. Design and Fabrication of Low-Cost Microfluidic Chips and Microfluidic Routing System for Reconfigurable Multi-(Organ-on-a-Chip) Assembly Micromachines (Basel) 2021, 12, 1542.

[25]. Ramadan Q.; Alawami H.; Zourob M. Microfluidic system for immune cell activation and inflammatory cytokine profiling: Application to screening of dietary supplements for anti-inflammatory properties Biomicrofluidics 2022, 16, 054105.

[26]. Nasrollahi S.; Banerjee S.; Qayum B.; Banerjee P.; Pathak A. Nanoscale Matrix Topography Influences Microscale Cell Motility through Adhesions, Actin Organization, and Cell Shape ACS Biomater Sci Eng. 2017, 3, 2980-2986.

[27]. Salpavaara, T.; Joki, T.; Skogberg, A.; Calejo, M. T.; Lekkala, J.; Narkilahti, S.; Kallio, P. Microfabricated porous SU-8 membranes as innervation interfaces for hiPSC-neurons in microfluidic devices J. Phys. Commun. 2021, 5, 115003.

[28]. Bhattarai RS, Bachu RD, Boddu SHS, Bhaduri S. Biomedical Applications of Electrospun Nanofibers: Drug and Nanoparticle Delivery Pharmaceutics. 2018, 11, 5.

[29]. Gonçalves AM.; Leal F.; Moreira A.; Schellhorn T.; Blahnová VH.; Zeiringer S.; Vocetková K.; Tetyczka C.; Simaite A.; Buzgo M.; Roblegg E.; Costa PF.; Ertl P.; Filová E.; Kohl Y.; Adv. NanoBiomed Res. 2023, 3, 2200104.

[30] Deng Y., Lu T., Cui J., Ma W., Qu Q., Zhang X., Zhang Y., Zhu M., Xiong R., Huang C., Morphology engineering processed nanofibrous membranes with secondary structure for high-performance air filtration Sep. Purif. Technol. 2022, 294, 121093.

[31]. Xue J.; Wu T.; Dai Y.; Xia Y. Electrospinning and Electrospun Nanofibers: Methods, Materials, and Applications. Chem Rev. 2019, 119, 5298-5415.

[32]. Fujihara K.; TeoWE.; Lim TC.; Zuwei Ma Z. An Introduction to Electrospinning and Nanofibers. World Scientific Publishing, 2005, 90.

[33]. Gonçalves AM.; Moreira A.; Weber A.; Williams GR.; Costa PF. Osteochondral Tissue Engineering: The Potential of Electrospinning and Additive Manufacturing. Pharmaceutics 2021, 13, 983.

[34]. Moghadas H.; Saidi MS.; Kashaninejad N.; Kiyoumarsioskouei A.; Nguyen NT.; Fabrication and characterization of low-cost, bead-free, durable and hydrophobic electrospun membrane for 3D cell culture Biomed Microdevices. 2017, 19, 74.

[35]. Moghadas H.; Saidi MS.; Kashaninejad N.; Nguyen NT.; A high-performance polydimethylsiloxane electrospun membrane for cell culture in lab-on-a-chip Biomicrofluidics. 2018, 12, 024117.

[36]. Mohammadzadeh L.; Rahbarghazi R.; Salehi R.; Mahkam M. A novel egg-shell membrane based hybrid nanofibrous scaffold for cutaneous tissue engineering J Biol Eng. 2019, 26, 79.

[37]. Cheng T.; Li S.; Xu L.; Ahmed A. Controllable preparation and formation mechanism of nanofiber membranes with large pore sizes using a modified electrospinning Mater. Des. 2019, 178, 107867.

[38]. Amores de Sousa MC.; Rodrigues CAV.; Ferreira IAF.; Diogo MM.; Linhardt RJ.; Cabral JMS.; Ferreira FC. Functionalization of Electrospun Nanofibers and Fiber Alignment Enhance Neural Stem Cell Proliferation and Neuronal Differentiation. Front Bioeng Biotechnol. 2020, 8:580135.

[39]. Krysiak ZJ.; Gawlik MZ.; Knapczyk-Korczak J.; Kaniuk Ł.; Stachewicz U. Hierarchical Composite Meshes of Electrospun PS Microfibers with PA6 Nanofibers for Regenerative Medicine. Materials (Basel). 2020, 13, 1974.

[40]. Jiang W.; Wang H.; Cui Y.; Lei Y.; Wang Y.; Xu D.; Jiang N.; Chen Y.; Sun Y.; Zhang Y.; Cao J.; Ke Z. Polymer nanofiber-based microchips for EGFR mutation analysis of circulating tumor cells in lung adenocarcinoma. Int J Nanomedicine. 2018, 13, 1633-1642.

[41]. Yang T.; Arnold JJ.; Ahsan F. Tetradecylmaltoside (TDM) enhances in vitro and in vivo intestinal absorption of enoxaparin, a low molecular weight heparin. J Drug Target. 2005, 13, 29-38.

[42]. Franco P.; De Marco I. The Use of Poly (N-vinyl pyrrolidone) in the Delivery of Drugs: A Review. Polymers (Basel). 2020, 12, 1114.

[43]. Koczkur KM.; Mourdikoudis S.; Polavarapu L.; Skrabalak SE. Polyvinylpyrrolidone (PVP) in nanoparticle synthesis Dalton Trans. 2015,44, 17883-17905.

[44]. Pablos JL.; Tiemblo P.; Ellis G.; Corrales T. Chloroaluminate Gel Electrolytes Prepared with Copolymers Based on Imidazolium Ionic Liquids and Deep Eutectic Solvent AlCl3:Urea. Polymers (Basel). 2021, 13, 1050.

[45]. Tan SH.; Inai R.; Kotaki M.; Ramakrishna S. Systematic parameter study for ultra-fine fiber fabrication via electrospinning process Polymer 2005, 46, 6128.

[46]. Fong H.; Chun I.; Reneker DH.; Beaded nanofibers formed during electrospinningPolymer 1999, 40, 4585.

[47]. Al-Azzam N.; Alazza A. Micropatterning of cells via adjusting surface wettability using plasma treatment and graphene oxide deposition PLoS One. 2022, 17, 0269914.

[48]. Ritter GS.; Dolgova EV.; Petrova DD.; Efremov YR; Proskurina AS.; Potter EA.; Ruzanova VS.; Kirikovich SS.; Levites EV.; Taranov OS.; Ostanin AA.; Chernykh ER.; Kolchanov NA.; Bogachev SS. The new general biological property of stem-like tumor cells Part I. Peculiarities of the process of the double-stranded DNA fragments internalization into stem-like tumor cells Front Genet. 2022, 13, 954395.

[49]. Radhakrishnan P.; Mathew RJ.; Krishnakumar G.; Sajeev US.; Interfacial electron transfer and modification of optical emission in Rhodamine 6G doped Polystyrene micro fibrous matrix by the incorporation of TiO2 nanoparticles Results in Optics 2021, 5, 100151.

[50]. Namsheer K.; Rout CS. Conducting polymers: a comprehensive review on recent advances in synthesis, properties and applications RSC Adv. 2021, 11, 5659.

[51]. Cha G.; Schmuki P.; Altomare M. Free-Standing Membranes to Study the Optical Properties of Anodic TiO2 Nanotube Layers Chem Asian J. 2016, 11, 789.

[52]. Ren J.; Isakova A.; Friedmann D.; Zeng J.; Grutzner SM.; Pun A.; Zhao GQ.; Kolluru SS.; Wang R.; Lin R.; Li P.; Li A.; Raymond JL.; Luo Q.; Luo M.; Quake SR.; Luo L. Single-cell transcriptomes and whole-brain projections of serotonin neurons in the mouse dorsal and median raphe nuclei Elife. 2019, 8, 49424.

[53]. Sajay B.N.G., Chiam S.Y., and Q. Ramadan Q., Optimization of micro-fabricated porous membranes for intestinal epithelial cell culture and *in vitro* modeling of the human intestinal barrier J. Micromech. Microeng. 2017, 27, 124004.

[54]. Bullen TF.; Forrest S.; Campbell F.; Dodson AR.; Hershman MJ.; Pritchard DM.; Turner JR.; Montrose MH.; Watson AJ. Characterization of epithelial cell shedding from human small intestine Lab Invest. 2006, 86, 1052.

[55]. Forsyth CB.; Shannon KM.; Kordower JH.; Voigt RM.; Shaikh M.; Jaglin JA.; Estes JD.; Dodiya HB.; Keshavarzian A. Increased intestinal permeability correlates with sigmoid mucosa alpha-synuclein staining and endotoxin exposure markers in early Parkinson's disease PLoS ONE 2011, 6, 28032.

[56]. Genser L.; Aguanno D.; Soula HA.; Dong L.; Trystram L.; Assmann K.; Salem J-E.; Vaillant J-C.; Oppert J-M.; Laugerette F. Michalski MC.; Wind P.; Rousset M.; Brot-Laroche E.; Leturque A.; Clément K.; Thenet S.; Poitou C. Increased jejunal permeability in human obesity is revealed by a lipid challenge and is linked to inflammation and type 2 diabetes J. Pathol. 2018, 246, 217.

[57]. McCreight Lj.; Baile CJ.; Pearson ER. Metformin and the gastrointestinal tract Diabetologia. 2016, 59, 426.

[58]. Innzucchi SE.; Lipska KJ.; Mayo H.; Bailey CJ.; McGuire DK. Metformin in patients with type 2 diabetes and kidney disease: a systematic review JAMA. 2014, 312, 2668.

[59]. Peters N.; Jay N.; Barraud D.; Cravoisy A.; Nace L.; Bollaert PE.; Gibot S. Metformin-associated lactic acidosis in an intensive care unit. Crit Care. 2008, 12, 149.

[60]. Weller A.; Hansen MB.; Marie R.; Hundahl AC.; Hempel C.; Kempen Paul PJ.; Frandsen HL. Parhamifar L.; Larsen JB.; Andresen T. Quantifying the transport of biologics across intestinal barrier models in real-time by fluorescent imagingFront. Bioeng. Biotechnol. 2022, 10, 33899.

[61]. Chou CH. Uptake and dispersion of metformin in the isolated perfused rat liver J Pharm Pharmacol. 2000, 52, 1011.

[62]. Nicklin P.; Keates AC.; Page T.; Bailey CJ. Transfer of metformin across monolayers of human intestinal Caco-2 cells and across rat intestine Int J Pharm. 1996, 128, 155.

[63]. Proctor WR.; Bourdet DL.; Thakker DR. Mechanisms underlying saturable intestinal absorption of metformin Drug Metab Dispos. 2008, 36, 1650.